



Laser powder bed fusion of molybdenum: Density, structure and mechanical properties at room and elevated temperatures

Aurore Leclercq, Thibault Mouret , Vladimir Brailovski ^{*} 

École de technologie supérieure, 1100 Notre-Dame West, Montréal, QC, H3C 1K3, Canada

ARTICLE INFO

Keywords:

Laser powder bed fusion
Molybdenum
Numerical predictions
Mechanical testing
Elevated temperature
Crack-free specimens
Geometric analysis

ABSTRACT

Molybdenum is a material of great industrial interest due to its specific properties, particularly at elevated temperatures. Additive manufacturing technologies have recently been proposed as an alternative to conventional powder metallurgy processes because of their flexibility in producing complex geometries. In this study, interrelations between the laser powder bed fusion process parameters and structural and mechanical properties of printed molybdenum specimens are investigated with a bid to propose an optimal set of process parameters. To support this approach, a plan of experiments was built using a simplified numerical simulation of the temperature field surrounding the melt pool. This approach led to the production of crack-free specimens with a printed density of 97 %, an ultimate strength of 510 MPa, a yield strength of 340 MPa, and a maximum strain of 11 % (all in compression at room temperature) using an optimized set of printing parameters $P = 179$ W, $v = 133$ mm/s, $h = 60$ μ m and $t = 30$ μ m. Compression testing in the 20–1000 °C temperature range revealed that the mechanical properties of printed molybdenum (ultimate strengths of 260 and 150 MPa at 800 and 1000 °C, respectively) are comparable to their conventional powder metallurgy manufactured counterparts. Printing of a series of geometric artifacts, such as walls (down to 0.1 mm in thickness), gaps (down to 0.3 mm in width) and lattice structures (50 and 60 % porosity gyroids), has proven the potential of laser powder bed fusion to produce complex molybdenum parts for applications over a wide temperature range.

1. Introduction

Molybdenum (Mo) is a transition metal belonging to the group of refractory metals with a high melting temperature ($T = 2896$ K/2623 °C). Its low thermal expansion coefficient ($\alpha_{(25-500\text{ }^\circ\text{C})} = 4.7\text{--}5.8 \cdot 10^{-6}$ /K) [1], high thermal conductivity (130–140 W/(m.K) [2,3], high mechanical properties [4,5] and excellent wear and corrosion resistance [6–10] make this metal and its alloys particularly interesting for industrial applications. Thanks to its high biocompatibility, corrosion resistance and strength and a reduced weight, as compared to some alternatives (tungsten and tantalum), molybdenum is also used in medical applications [11,12]. In the petrochemical industry [13,14], like other refractory metals, molybdenum is mainly used as a metal catalyst for selective reactions, but it is also employed within equipment parts exposed to severe corrosive environments. The mechanical properties of molybdenum at elevated temperatures (ultimate tensile strength ~ 210 MPa [4] and Young's modulus ~ 280 GPa at 800 °C [15]) are exceeded only by those of tungsten, but for almost twice the density (10.2 g/cm³ for Mo versus 19.2 g/cm³ for W [16]), making molybdenum appealing for the aerospace, defense

and energy [17–21] applications. Finally, molybdenum and its alloys are noteworthy materials in the nuclear safety field. Their ability to absorb neutrons and their high thermochemical compatibility allow to improve the corrosion resistance of parts such as fuel claddings of light water reactors (LWRs) and fast neutron reactors (FNRs) [22–24].

Nowadays, conventional processes, such as those associated with powder metallurgy, followed by additional steps (forging, machining, etc.), remain the most common way to produce semi-finished refractory products such as sheets, rods, wires and tubes. To produce more complex geometries, joining and subtractive processes are used, but their application is hindered by technical issues: during welding, the molybdenum affinity to oxygen risks severe degrading the heat affected zone [25], and during material removal, the elevated hardness of molybdenum significantly increases machining costs [26]. To produce complex geometries, additive manufacturing (AM) technologies help overcoming these limitations, thereby offering a promising solution. Furthermore, the recycling of unmelted powders allows to significantly decrease overall processing costs associated with such expensive materials. During the last decades, different AM technologies were used to produce parts from

* Corresponding author.

E-mail addresses: aurore.leclercq.1@ens.etsmtl.ca (A. Leclercq), thibault.mouret@etsmtl.ca (T. Mouret), vladimir.brailovski@etsmtl.ca (V. Brailovski).

<https://doi.org/10.1016/j.msea.2025.148004>

Received 19 November 2024; Received in revised form 30 January 2025; Accepted 5 February 2025

Available online 7 February 2025

0921-5093/© 2025 The Authors. Published by Elsevier B.V. This is an open access article under the CC BY license (<http://creativecommons.org/licenses/by/4.0/>).

refractory metals and alloys [27,28]. One such technology is the layer-by-layer laser powder bed fusion (LPBF), which applies a laser heat source to sequentially melt one powder layer at a time following a selected pattern corresponding to a sliced 3D-CAD volume of the part to be fabricated. As compared to its principal competitor, electron-beam powder bed fusion (EB-PBF), LPBF stands out due to its higher resolution, printing flexibility and a relatively lower cost [29,30]. Multiple recent publications have covered the use of the LPBF process to produce 3D printed parts from different refractory metals, including tungsten, molybdenum, niobium and tantalum [3,31–33]. While the printing of any refractory metal poses significant challenges related to their extremely high melting points, the present work focuses on the printability of pure molybdenum.

To overcome the issues reported for molybdenum LPBF printing, strategies are commonly established to mitigate the high sensitivity of molybdenum to hot and cold cracking. As well as the former is concerned, a study [34] have highlighted the fundamental role of impurities on the cracking susceptibility of refractory metals. Despite the inert atmosphere in the printing chamber, some residual oxygen enables molybdenum to form oxide MoO_2 which segregates at grain boundaries (GB) during the solidification step due to the low oxygen solubility of body-centered cubic molybdenum. The remaining liquid phase becomes enriched in oxygen and cannot withstand the thermal stresses and strains induced by the process [35]. Since these impurities segregate at GB, the cohesion of the latter decreases, thus leading to their embrittlement. This phenomenon, combined with high temperature gradients and cooling rates accompanying the process, also increases the risk of cold cracking [34,36].

The above issues inherent to molybdenum highly complicates its 3D printing process. According to the current state of the art, fully dense and crack-free parts are extremely difficult to obtain on printers with power-limited laser sources ($P_{\text{max}} \leq 200$ W). Only a few authors have claimed to have achieved printed densities greater than 98 % with small printers (EOS M100 and SLM-50) [3,37]. Apart these cases, printed density reported for small printers is often quite low (between 50 and 90 %) [38,39]), and that despite the use of extremely high volumetric energy densities (VED (1) up to 1000 J/mm^3) and low building rates (BR (2) down to $0.35 \text{ cm}^3/\text{h}$). Note that these last two metrics conveniently aggregate the following process parameters: laser power P (W), scanning speed v (mm/s), hatching space h (mm) and layer thickness t (mm).

$$VED [\text{J/mm}^3] = \frac{P}{vht} \quad (1)$$

$$BR [\text{cm}^3/\text{h}] = vht \quad (2)$$

The use of more powerful printers ($P = 400$ W) appeared to be the solution to increase printed density to up to 99.9 %. However this increase in printed density was frequently achieved at the cost of persisting microcracks [40,41]. In addition to the tight control of the printing atmosphere, two technical solutions have been identified and tested in an attempt to prevent the microcrack formation. The first and the more evident solution is to preheat either the build plate or the powder bed to reduce thermal stresses. While direct preheating of the build plate has been reported to be highly ineffective, regardless of the preheating temperature (400 °C in Ref. [42] and 1000 °C in Ref. [34]), laser preheating of the powder bed has shown its efficiency to reduce the microcrack formation. Another technical solution focuses on the optimization of printing parameters or the scanning strategy to control the microstructure and accommodate the thermal stresses generated by the process. An extensive study [40] using a wide range of parameters highlighted the evolution of the crystallographic texture as a function of process parameters, but did not report any beneficial effect on the cracking occurrence, regardless of the microstructure orientation obtained. Other studies have reported some improvements achieved by modifying the rotational angle between layers [43] and by optimizing

the design of support structures [44]. However, all these solutions have apparently been insufficient to produce parts that are both dense and crack-free.

To better understand and optimize the process, different numerical tools of various complexity have been developed. To account for the majority of physical phenomena accompanying the LPBF process (solidification, evaporation, condensation, etc.) and determine the optimum powder characteristics and process parameters, some authors proposed 3D coupled thermo-fluid dynamical simulation models [45, 46]. More recently, to simulate the printing of pure molybdenum, a coupled discrete elements model (DEM) and computational fluid dynamics (CFD) model was developed [47]. The simulation results were then used with a machine learning algorithm to generate a process map considering both the powder bed and the molten track quality. However, such complex models are time- and computer resource-intensive, and their calibration is extremely delicate. While these simulation tools are useful for detailed studies of physical phenomena underlying the process, they are not well-suited for the process optimization purposes, in which case simpler models are preferred. As an example, Bajaj et al. [48] used an analytical heat transfer model to estimate the melt pool dimensions formed by a pulsed laser in high thermal conductivity alloys, including molybdenum. Following correlations with the experimental results, the authors were able to identify the processing window allowing to print high-density crack-free parts (~97 %) using a reduced layer thickness of $20 \mu\text{m}$.

The present study follows the same cost-effective path of process optimization via the application of a simplified model of the thermal field created by a moving laser source. The melt pool calculations are used to design the experiment and study the effects of process parameters on the structure and mechanical properties of printed parts, with an ultimate goal of optimizing the process parameters. In anticipation of high temperature applications of printed parts, the optimized process parameters are then used to print specimens for testing in the 20 – 1000 °C temperature range. The same optimized process parameters are also applied to print a series of geometric artifacts, such as walls, gaps and lattice structures, in order to demonstrate the ability of the process to produce complex geometries of potential industrial interest.

2. Materials and methods

The developed workflow aims to cover different process development phases, including powder characterization, process simulation and the establishment of an experimental setting. These phases are followed by a study of interrelations between the process parameters, the density, the microstructure and the mechanical properties of printed specimens. The final phase of the workflow involves the selection of an optimized set of process parameters, compression testing over a large temperature range, and the printing of a series of geometric artifacts representative of some potential applications.

2.1. Powder characterization

Plasma-spheroidized molybdenum powder ($\text{Mo} > 99.9\%$, $\text{O} \leq 500$ ppm, Hall flow $\leq 15 \text{ sec./50g}$) used in this study was produced by Tekna Co. Ltd. (Sherbrooke, Canada). The particle size distribution of $D_{10} = 12.6$, $D_{50} = 20.6$ and $D_{90} = 32.0$ (μm) was measured using a Beckman Coulter LS13 320 XR (Brea, CA, USA) particle size analyzer equipped with a water module, and the particle morphology was observed using a Hitachi TM3000 (Tokyo, Japan) scanning electron microscope (Fig. 1a and b). The rheological properties of the powder were measured using an FT4 powder rheometer (Freeman Technology, UK) and collected in Table 1. Based on these measurements, it can be asserted that the selected powder presents good flowability and is suitable for laser powder bed fusion additive manufacturing [49].

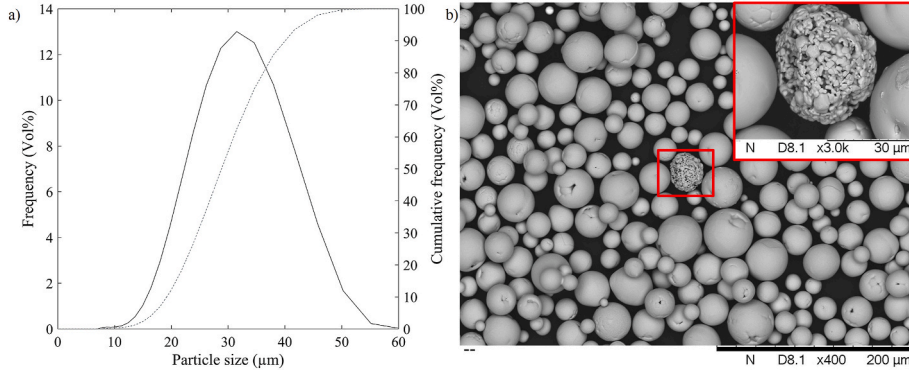


Fig. 1. Geometry characteristics of molybdenum powder: a) particle size distribution and b) particle morphology.

Table 1

Rheological properties of molybdenum powder (indexes adopted from Ref. [49]): BD (Bulk Density), CI (Compressibility Index), PD (Pressure Drop), SE (Specific Energy), AE10 (Aeration Energy at 10 mm/s air velocity) BFE (Basic Flow Energy), CC (Cohesion Coefficient).

BD (g/cm ³)	CI (%) at 15 kPa	PD (mBar) at 15 kPa	SE (mJ/g)	AE ₁₀ (mJ)	BFE (mJ)	CC (kPa)
6.04 (±0.47 %)	7.65 (±6.57 %)	8.31 (±8.51 %)	2.53 (±2.65 %)	10.60 (±6.21 %)	1084 (±1.23 %)	0.33

2.2. Experiments and equipment

To limit the number of specimens needed to study the effects of process parameters on the density, structure and mechanical properties of printed molybdenum, a plan of experiments was built with the help of a melt pool model successfully tested with tungsten powders in Ref. [33].

2.2.1. Numerical model of the melt pool

The numerical model [33] used in this work was developed in the MATLAB software (R2022b, MathWorks, USA) environment. This model calculates the melt pool dimensions on the basis of analytical calculations of the temperature field generated by a moving Gaussian heat source in a semi-infinite solid ((3)–(5)):

$$T(x, y, z) = T_0 + \frac{AP}{kr_f \pi^{3/2}} \int_{-\infty}^0 \frac{1}{1 + \tau^2} \exp(C) d\tau \quad (3)$$

with

$$C = -\left(\frac{\tau^2}{1 + \tau^2}\right) \left(\left(\xi - \frac{Pe}{2\tau^2} \right)^2 + \eta^2 \right) - \tau^2 \zeta^2 \quad (4)$$

$$\xi = \sqrt{2} \frac{x}{r_f}; \quad \eta = \sqrt{2} \frac{y}{r_f}; \quad \zeta = \sqrt{2} \frac{z}{r_f}; \quad (5)$$

$$Pe = \frac{r_f v}{2\sqrt{2}\alpha}; \quad \tau = \frac{r_f}{2\sqrt{2}adt}; \quad \alpha = \frac{k}{\rho c_p}$$

where T_0 is the baseplate temperature (K); A , the absorptivity; P , the laser power (W); k , the thermal conductivity (W/(m.K)); r_f , the laser beam radius (m); Pe , the Peclet number; v , the scanning speed (m/s); α , the thermal diffusivity (m²/s); ρ , the density (kg/m³); c_p , the mass heat capacity (J/(kg.K), and dt , the time (s).

Knowing that during the LPBF process, the feedstock material is not solid, but forms a powder bed, some variables need to be corrected, namely.

- The density, using (6):

$$\phi = 1 - CBD; \quad CBD = \frac{BD}{\rho_s} \quad (6)$$

where ϕ is the fractional porosity; CBD , the coefficient of bulk density

(without unit); ρ_s , the material density (kg/m³) and BD (kg/m³), the bulk density measured using an FT4 powder rheometer (Table 1).

- The absorptivity ((7)–(9)) [50] is calculated using the Hagen-Rubens model approximating the material absorptivity using its electrical resistivity value:

$$\epsilon_{powder} = S_h \epsilon_h + (1 - S_h) \epsilon_s \quad (7)$$

with

$$\epsilon_s = A = 0.365 \left(\frac{R_s}{\lambda} \right)^{0.5} \quad (8)$$

and

$$S_h = \frac{0.908\phi^2}{1.908\phi^2 - 2\phi + 1}; \quad \epsilon_h = \frac{\epsilon_s \left(2 + 3.082 \left(\frac{1-\phi}{\phi} \right)^2 \right)}{\epsilon_s \left(1 + 3.082 \left(\frac{1-\phi}{\phi} \right)^2 \right) + 1} \quad (9)$$

where ϵ_{powder} is the powder emissivity (absorptivity); S_h , the surface fraction occupied by pores; ϵ_h , the pores emissivity; ϵ_s , the emissivity of a bulk material, R_s ; the electrical resistivity of the material (Ω.m) and λ , the laser wavelength (m).

- The thermal conductivity (10), following the work of [51]:

$$k_{powder} = k_s (1 - \phi)^{\frac{4}{3}} \quad (10)$$

where k_{powder} and k_s are the thermal conductivities (W/(m.K)) of a powder bed and a bulk material, respectively.

It is clear that during LPBF, the thermal conductivity, the specific heat capacity and the laser absorptivity vary from their values at room temperature to those near the melting point. Since in this model, the material properties are considered constant, it is necessary to find which values must be used to obtain relevant results. To find these values, the model was tested with different sets of the temperature-dependant properties. This study consisted of a series of melt pool simulations, with the material properties varying from their room temperature (RT) to their melting temperature (TM) values (Table 2).

Results of the melt pool calculations were then compared with their experimental equivalents [3,52] to select the temperature at which these

Table 2

Properties variation ranges considered as model inputs: Material density is taken from Ref. [4]; powder bed density is extracted from the rheometer test (BD, Table 1); Dense material: Specific heat capacity, thermal conductivity and electrical resistivity extrapolated from Ref. [15] and absorptivity calculated using equation (8); Powder bed: Thermal conductivity and absorptivity are calculated using equations (7)–(10).

Temperature of Application (K)	State of Matter	Density (kg/m ³)	Specific Heat Capacity (J/(kg·K))	Thermal Conductivity (W/(m·K))	Electrical Resistivity (nΩ·m)	Absorptivity (%)
Sensitivity study 293 (RT) – 2883 (TM)	Dense	10220	RT	TM	RT	TM
	Powder	6040	255	411	141	56
					70	28
Selected values 0.8 (TM) or 2306	Powder	6040	376	37	590	42

material properties provide the smallest discrepancies between the calculated and measured melt pool sizes. It was found that if the material properties were taken at 0.8TM, the modeled and experimental melt pool sizes were the closest (the same result was obtained for pure tungsten in the reference work). As an illustration, results of the regression analysis between the calculated and experimentally-measured melt pool widths are presented in Fig. 2a with a directive coefficient of unity, the negligible constant term, $R_{adj}^2 = 0.83$, $RMSE = 5$, and without any pattern in the residuals. Also, it can be observed that the more continuous the experimentally measured melt tracks, the closer the model predictions were to the experiment. A visual example of the comparison between the calculated and experimentally-measured melt pool widths is given in Fig. 2b and c for a specific case of $P = 130$ W, $v = 500$ mm/s and $r_f = 20$ μm, with an initial temperature of 80 °C, and the model properties taken at 0.8TM.

Finally, melt pool dimensions are linked to process parameters through the dimensionless metrics illustrated in Fig. 3a and b (i.e., melt pool depth-to-layer thickness ratio (D/t) and melt pool width-to-hatching space ratio (W/h)), and the latter are used to predict the printed density using a calibrated polynomial function taken from Ref. [33] (Fig. 3c). These density predictions are presented in the form of “printed density process map” in the volumetric energy density (VED , J/mm³)-build rate (BR , cm³/h) coordinates. Each map is built for one specific layer thickness and one specific hatching space, by varying the laser power and the scanning speed within the printer capacity limits. An example of such a map is given in Fig. 3d for a TruPrint 1000 system (TRUMPF GmbH, Ditzingen, Germany), with the laser power varying from 20 to 200 W and the scanning speed varying from 20 to 2000 mm/s. In this case, the layer thickness and hatching space are set at 30 and 80 μm, respectively. These density maps are used to build the plan of experiments presented in the following section.

2.2.2. Impact of process parameters on the density, structure and properties of printed specimens

To study the impact of process parameters on the density, structure and mechanical properties of printed specimens, five identical $VED-BR$

sets (A, B, C, D and E (Table 3)) were selected on five different process maps with a fixed layer thickness of 30 μm and an incrementally increasing hatching space, namely $h = 40, 60, 80, 100$ and 120 μm. These five process parameter sets were selected to cover the 70–99 % printed density range. The specimens were named according to the $VED-BR$ sets and hatching spaces selected. For example, specimen A-40 corresponds to the specimen obtained with a $VED-BR$ set of 1170 J/mm³ & 0.43 cm³/h and a hatching space of $h = 40$ μm (Table A.1 in the appendix provides the detailed plan of experiments, as well as the predicted densities.).

To conduct this experiment, twenty-five 10 mm-diameter, 21 mm-high cylindrical specimens with 5 mm dense supports were printed on a stainless-steel baseplate without preheating (Fig. 4a). The printed specimens were removed by hand from the baseplate using a hammer and chisel, their supports were cut off, and the remaining parts partitioned to obtain samples for structural analyses and compression testing at room temperature (Fig. 4b). Therefore, one specimen per each set of process parameters was produced and analyzed. Based on the results of this analysis (described in Section 3.3.1), one of the parameters sets of Table 3 was selected as being the best, and was then used to produce ten 10 mm-diameter, 21 mm-high cylindrical specimens for compression testing at elevated temperatures (600, 800 and 1000 °C).

2.2.3. Density measurements

Previous studies [33,53] highlighted that Archimedes measurements are not always suitable for LPBF-processed parts because of the possible presence of unmelted particles inside the pores, giving the false impression of a highly dense and therefore potentially highly resistant material. Moreover, the high density of molybdenum (10.22 g/cm³) limits the use of X-ray tomography for the porosity detection in parts printed with it. Because of these considerations, the density of printed samples was measured using images of their z-y cross-sections (Fig. 5). To this end, samples were mounted in carbon-doped resin, mirror-polished, and observed with a LEXT OLS4100 (Lext Olympus Corporation, Tokyo, Japan) laser confocal microscope. These observations enabled the

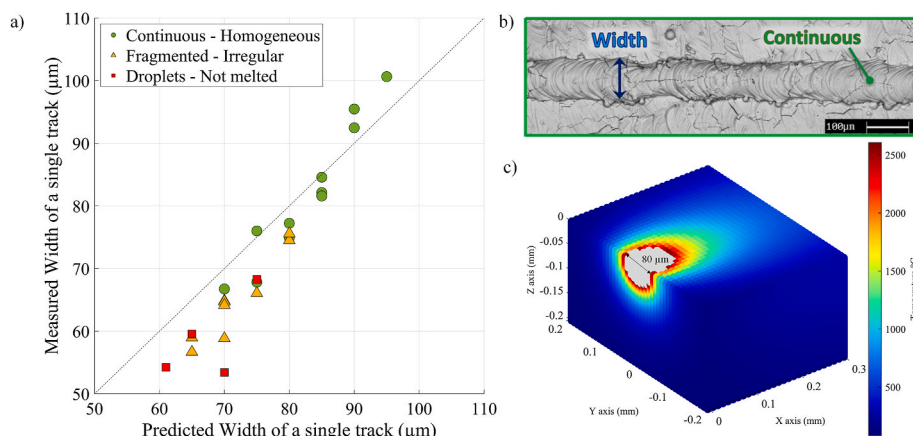


Fig. 2. a) Comparison between the measured [3,52] and calculated melt pool widths for pure molybdenum with 95 % confidence margins; b) photo of a single laser track extracted from Ref. [3] ($P = 130$ W, $v = 500$ mm/s, $r_f = 20$ μm) and c) calculated temperature field of the melt pool with properties taken at 0.8TM (Table 2).

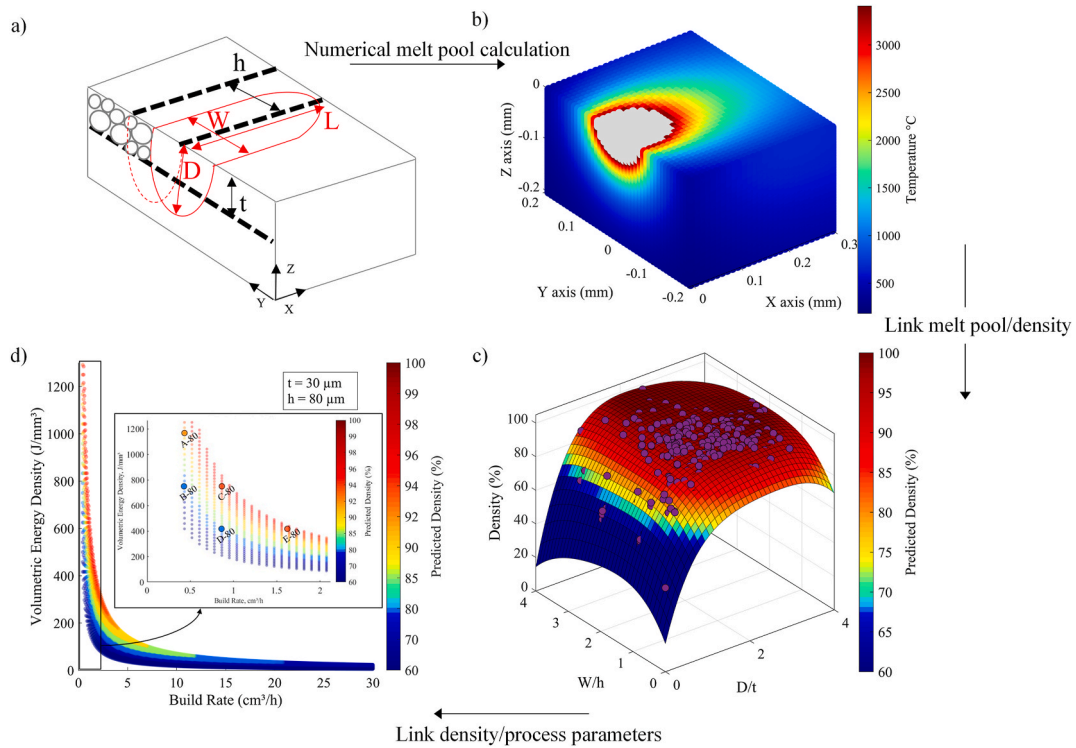


Fig. 3. a) Schematic representation of the melt pool, melt pool dimensions (depth D , width W and length L) and process variables (layer thickness t and hatching space h); b) example of the calculated (0.8TM) melt pool for pure molybdenum, c) response surface of the polynomial function relating printed density to dimensionless melt pool metrics (experimental points in purple dots) [33] and d) example of the density map for molybdenum ($t = 30 \mu\text{m}$, $h = 80 \mu\text{m}$) with the selected five VED-BR experimental sets for a TruPrint 1000. (For interpretation of the references to color in this figure legend, the reader is referred to the Web version of this article.)

Table 3
Parameter sets definition.

	A	B	C	D	E
VED, J/mm^3	1170	750	750	400	400
BR, cm^3/h^1	0.43	0.43	0.86	0.86	1.62

detection of defects (pores and cracks) larger than $3 \mu\text{m}$ in size (if no such defects were observed, samples are called crack-free). The obtained raw images (Fig. 5ac) were binarized (Fig. 5bd) in the MATLAB environment (R2022b, MathWorks, USA) using the grey level threshold which was locally adjusted considering the mean intensity (first-order statistics) in the vicinity of each pixel. Finally, the ratio of white-to-black pixels, *i.e.*,

the ratio of solid matter to void, was calculated. The density value retained for each sample corresponded to a mean value obtained from 3 observations and this measurement routine was validated by comparison with the results of manual segmentations in the ImageJ software environment.

In addition to the printed density, the image observations were used to characterize pore populations in terms of pore density (pores/ mm^2), size (equivalent diameter (11) in μm) and shape (circularity (12), without unit). According to the microscope resolution ($1 \text{ px} = 2.5 \mu\text{m}$), segmented defects with $\text{DE} < 20 \mu\text{m}$, which represented $\sim 5\%$ in terms of the cumulative pore surface area, were removed from the analysis. It enabled focusing the study on pores having the greatest impact on the mechanical properties.

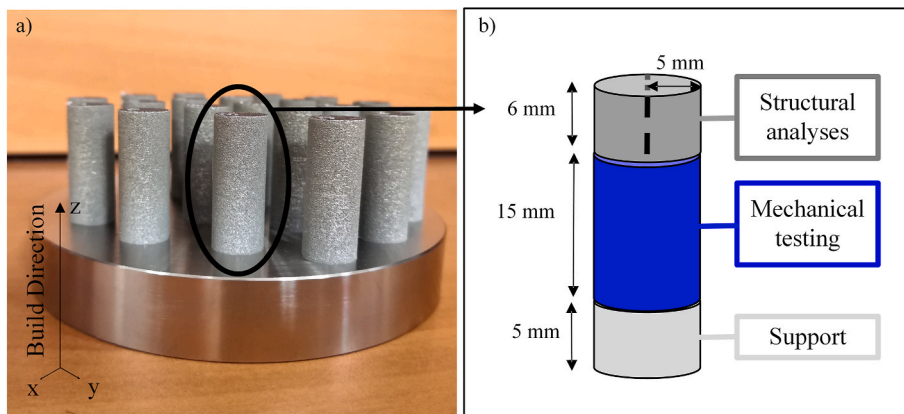


Fig. 4. a) Photo of a baseplate with printed specimens; b) schematic representation of a printed specimen with samples for structural analyses and mechanical testing.

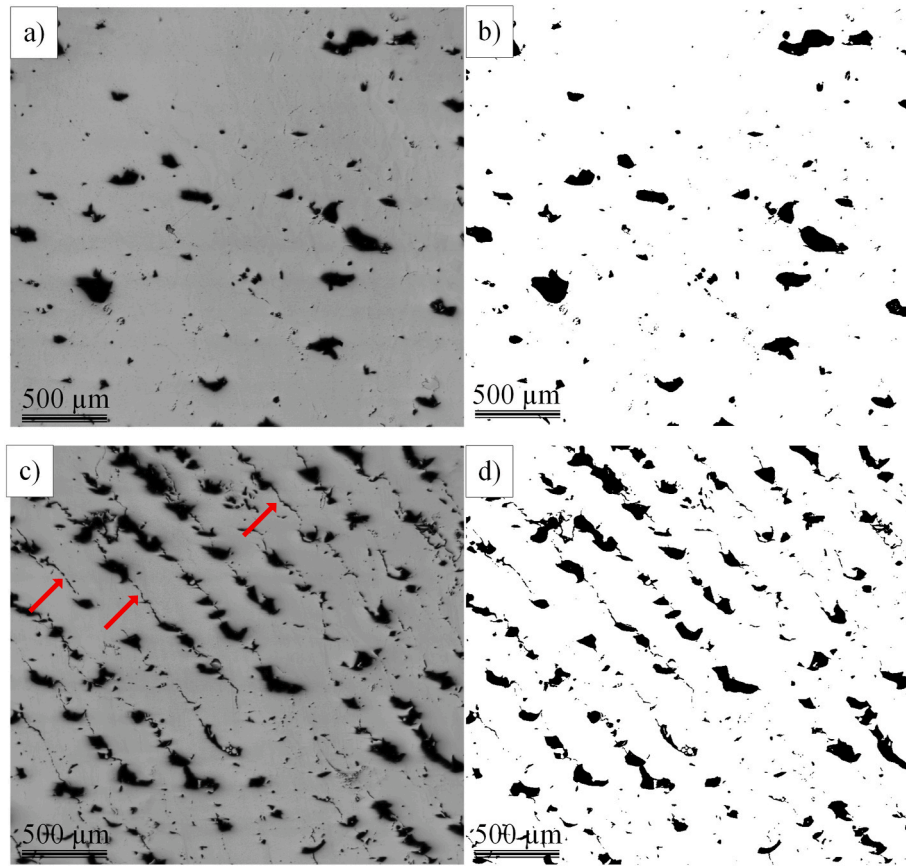


Fig. 5. C-60 specimen (z-y cross-section): a) microscopic image; b) binarized image (density $d = 97\%$, pore population 40 p/mm^2 , $DE50_p = 82 \mu\text{m}$ and $C50_p = 0.55$; C-40 specimen: c) microscopic image (z-y cross-section, cracks are shown by red arrows); d) binarized images (density $d = 89\%$, pore population 100 p/mm^2 , $DE50_p = 100 \mu\text{m}$ and $C50_p = 0.30$). (For interpretation of the references to color in this figure legend, the reader is referred to the Web version of this article.)

$$\text{Equivalent Diameter (DE)} = \sqrt{\frac{4\text{Area}}{\pi}} \quad (11)$$

$$\text{Circularity (C)} = \frac{4\pi\text{Area}}{\text{Perimeter}^2} \quad (12)$$

2.2.4. Microstructure and phase analyses

Microstructure analyses of the as-built specimens were carried out using electron backscatter diffraction (EBSD) inspection of their z-y cross-sections. To this end, mounted samples were first subjected to ion milling using a Hitachi EM 4000 plus (5 kV, 25 rpm, 15 min). The EBSD maps were built using a Hitachi SU-8230 Field Emission-STEM and then post-treated using the MATLAB software MTEX library. First, the Band Contrast (BC) metric was used to qualify the EBSD pattern quality. This metric is derived from the average intensity of Kikuchi bands with respect to the overall intensity within an EBSD pattern. It is evaluated by different levels of brightness going from 0 (bad EBSD pattern quality, black color) to 255 (good quality, white color). Unstrained materials would show higher-quality EBSD patterns, *i.e.*, light-colored maps, while the presence of defects would obscure the maps. The quality of the samples can therefore be compared by plotting the BC statistical distributions [54].

Next, the MacKenzie distributions were plotted to address the texture and the presence of substructures [55]. In this context, two groups of structural elements were identified as Low Angle Grain Boundary (LAGB) elements, having misorientation angles between 2 and 10° , and High Angle Grain Boundary (HAGB) elements, with misorientation angles larger than 10° . The LAGB and HAGB quantifications were carried out using their respective densities (μm^{-1}), which correspond to the boundary length divided by the indexed area [56,57]. Structures

corresponding to the HAGB elements were then used to assess the grain size, shape, orientation and distribution, following the procedure defined in the E2627-13 ASTM standard [58]. The grain size and shape metrics were obtained by analogy with those of pores and are referred herein to as the grain density, *i.e.*, the number of grains per mm^2 (grains/ mm^2); the grain size $DE10g$, $DE50g$ and $DE90g$ (μm), and the grain circularity, $C10g$, $C50g$ and $C90g$.

Finally, the extent of oxidation occurring during printing and high temperature mechanical testing was assessed by X-ray diffraction (XRD) analysis (X'Pert3 system equipped with a cobalt source, Malvern Panalytical Ltd, Malvern, UK), and the energy dispersive spectroscopy (EDS) technique (Hitachi SU-8230).

2.2.5. Mechanical testing at room and elevated temperatures

All printed specimens were subjected to room-temperature compression testing using an Alliance RF/200 testing machine (MTS, Eden Prairie, MN, USA) according to the E9-09 ASTM standard [59]. The compression rate was set at 0.01 mm/s and two high-resolution cameras were placed in front of the specimens to monitor the fracture mode during the tests. The force was measured using a 200 kN MTS load cell, while the displacement was measured using an LVDT. Based on these measurements, strain-stress diagrams were plotted to obtain the following metrics: Ultimate Compression Strength (UCS, MPa), defined as the maximum stress reached during the test, Yield Strength (YS, MPa), calculated by moving the slope from origin to 0.2% on the strain axis and Strain under maximum load (δ , %), representing the difference between the total compression strain at UCS and the elastic strain to failure.

High temperature compression testing of the selected specimens was carried out on an MTS 810 (MTS, Eden Prairie, MN, USA) load frame

under an argon flow of 27.5 ft³/h, with the force measured by a 100 kN MTS load cell and the displacement measured by an LVDT. The compression rate was set to 0.075 mm/min as per the ASTM E209-18 standard [60] and the temperature in the testing chamber was controlled using an infrared (IR) furnace. To ensure that the temperature in the core of the tested samples corresponded to that in the thermal chamber, one of the samples was instrumented with a K-type thermocouple and subjected to a controlled temperature rise up to 800 °C with a heating rate of 10 °C/min without applying stress. This enabled the validation of the temperature ramp and the establishment of a 3 min prior-to-testing dwell time. Three samples were compressed for each testing temperature and stress-strain diagrams were plotted and analyzed using the same procedure as that for the room-temperature testing.

2.2.6. Printability of complex structures

The optimized set of printing parameters was used to produce three geometric artifacts, namely the wall and gap artifacts with a thickness varying from 0.1 to 2 mm (adapted from Ref. [61], Fig. 6a,b,d) and 10 mm-diameter, 20 mm-high, 50 and 60 % porosity gyroid lattice structures (strut size respectively 345 and 240 μm) (Fig. 6c and d). For all of them, the contours were printed using the same parameters as the body, and the laser offset was kept to zero during the print. The gap and wall artifacts were subjected to optical measurements using a Keyence VHX7000, while the density of the gyroid lattice structures was measured using the Archimedes technique.

3. Results

3.1. Printed densities and pore structures

The predicted printed densities are plotted as functions of the process parameters in Fig. 7a. For all printing sets, the predicted density monotonously increases to reach a maximum value at $h/t = 2.5$ and then decreases. The highest densities (98–99 %) are predicted for the C (750 J/mm³; 0.86 cm³/h) and E (400 J/mm³; 1.62 cm³/h) VED-BR sets, while the lowest densities (91–93 %), are predicted for the B (750 J/mm³; 0.43 cm³/h) and D (400 J/mm³; 0.86 cm³/h) VED-BR sets, with the VED-BR set A (1170 J/mm³; 0.43 cm³/h) occupying the intermediate position.

For comparison, the effective (image-measured) printed densities are

plotted in Fig. 7b. It can be observed that for any h/t ratio, with the exception of $h/t = 1.3$, the C and E VED-BR sets also lead to the highest printed densities (up to 96 %), while the B and D VED-BR sets lead to the lowest printed densities (down to 87 %). As for the A VED-BR set, it leads to intermediate density values, oscillating between 92 and 94 %.

While the overall trends for the predicted and effectively measured printed densities are coinciding, two major discrepancies can be noted. The first is related to the printed density ranges, which are 91–99 % (simulations) versus 87–96 % (experiment), meaning that the model significantly overestimates the printed density. The second, more significant discrepancy is that for the two best VED-BR sets (C and E), when h/t increases, the density first increases to reach a maximum at $h/t = 2–2.7$ and then decreases to reach a minimum at $h/t = 3.3$, and finally, increases again to $h/t = 4$. The reasons why the model is not capable of predicting such a complicated density evolution are discussed in Section 4.1.

Based on the experimentally obtained data, it can be stated that the processing conditions leading to the highest printed densities (~97 %), and therefore to potentially higher mechanical properties, correspond to the following printing parameters $P = 179$ W, $v = 133$ mm/s, $h = 60$ μm and $t = 30$ μm (C-60 set with $h/t = 2$). Further, the printing parameters $P = 180$ W, $v = 125$ mm/s, $h = 120$ μm and $t = 30$ μm (E-120 with $h/t = 4$) leading to a printed density of ~96 % should not be removed from consideration.

The porosity study revealed the pores population in the [30; 121] p/mm² range, with a median circularity $C50_p = [0.30; 0.55]$ and a median pore size $DE50_p = [65; 100]$ μm. No clear trends can be observed with any of the porosity metrics in respect to the process parameters. Concerning the parameter sets C-60 and E-120 leading to the best measured densities (Fig. 8), the C-60 samples contain slightly larger pores than their E-120 counterparts: $[DE50_p; DE90_p] = [82; 120]$ μm for the former versus $[DE50_p; DE90_p] = [70; 110]$ μm for the latter. However, the density (40 pores per mm²) and circularity ($C50_p = 0.55$) of pores are similar in both cases.

3.2. Crystalline phases and microstructures

Immediately following the printing, selected specimens were subjected to XRD analyses to detect traces of oxidation that may have occurred during the process. The XRD measurements conducted on samples C-60 and E-120 revealed only the bcc structure of pure molybdenum. To compensate for the detection limits of this technique,

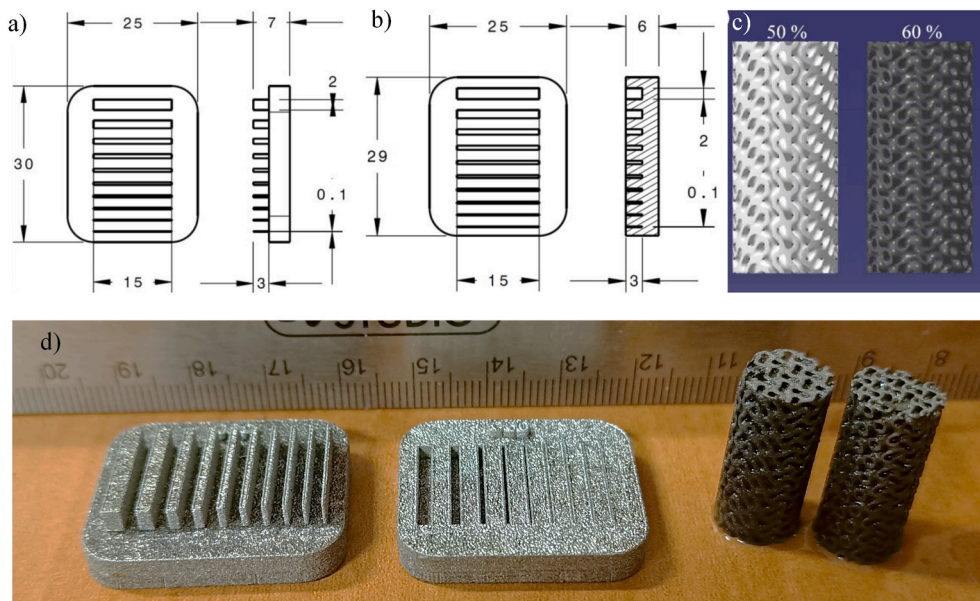


Fig. 6. Drawings of the printed geometric artifacts: (a) walls, (b) gaps, (c) 50 and 60 % porosity gyroid lattice structures; (d) printed artifacts.

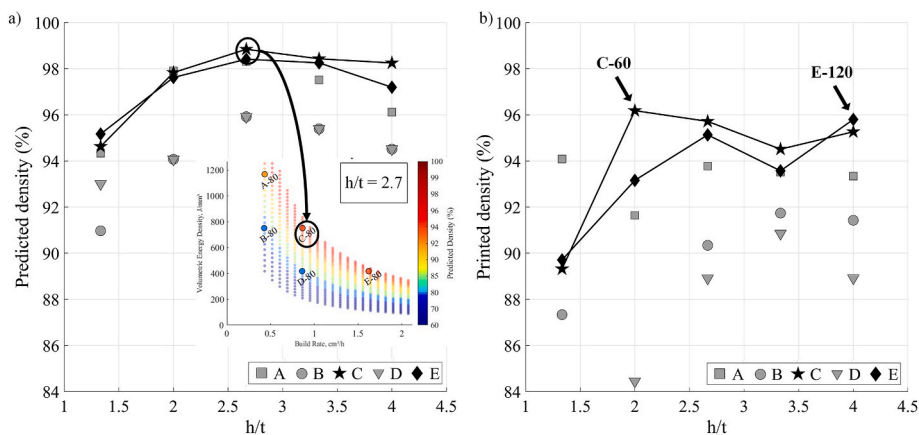


Fig. 7. a) Predicted and b) measured printed densities for different process parameters sets (arrows point to the C-60 and E-120 sets leading to the highest measured printed densities).

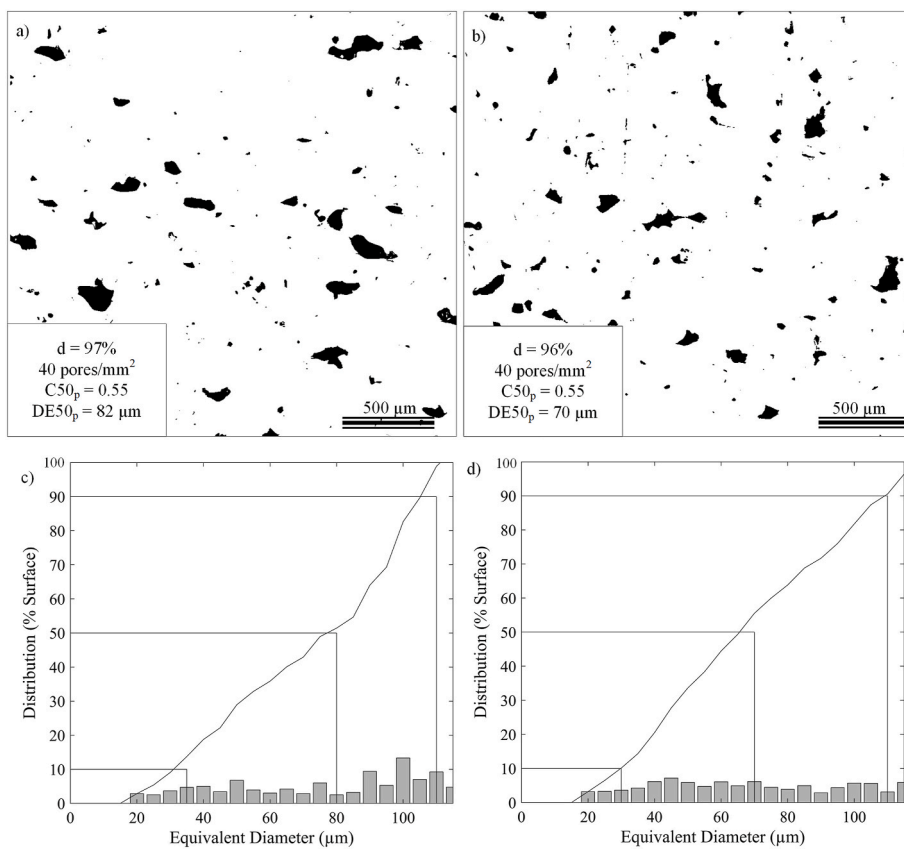


Fig. 8. Binarized surfaces of the samples a) C-60 and b) E-120 with segmented pores and their pore distributions: c) C-60 and d) E-120.

some additional investigations were conducted on the cross-polished sections and compression fracture surfaces, using the SEM and EDX techniques (Fig. 9). For all the parameter sets, these analyses detected some minor oxidation traces. Furthermore, observations made on the polished cross-sections demonstrated a higher concentration of oxygen at the grain boundaries. This is consistent with the related literature [34, 36], which describes the tendency of molybdenum to have impurities segregating at these interfaces. However, such visual observations do not allow comparing the overall oxidation levels between the two different sets of parameters (C-60 and E-120).

The EBSD analyses were carried out on samples C-60 and E-120 with the highest printed densities. For both samples, the BC maps were relatively light-colored and showed no clear difference between them, as

highlighted in Fig. 10a and b. The statistical distributions obtained show one peak at BC = 160 (Fig. 10c), which reflects the presence of only one phase in both samples. It should be noted that an increase in the h/t ratio leads to a slight shift of this peak to the left, meaning a small decrease in the pattern quality, and thus, a higher presence of defects or internal stresses. Then, the MacKenzie plots of misorientation angles (Fig. 10d) are similar to those of conventional polycrystalline cubic materials with random texture [55]. This absence of preferential orientation was also confirmed by the pole figures presented in Fig. 10e. Also, these diagrams revealed a significant population of structural elements with small misorientation angles (LAGB, $<10^\circ$), thus revealing the presence of substructures accommodated by arrays of dislocations.

The boundary density values of the LAGB and HAGB structural

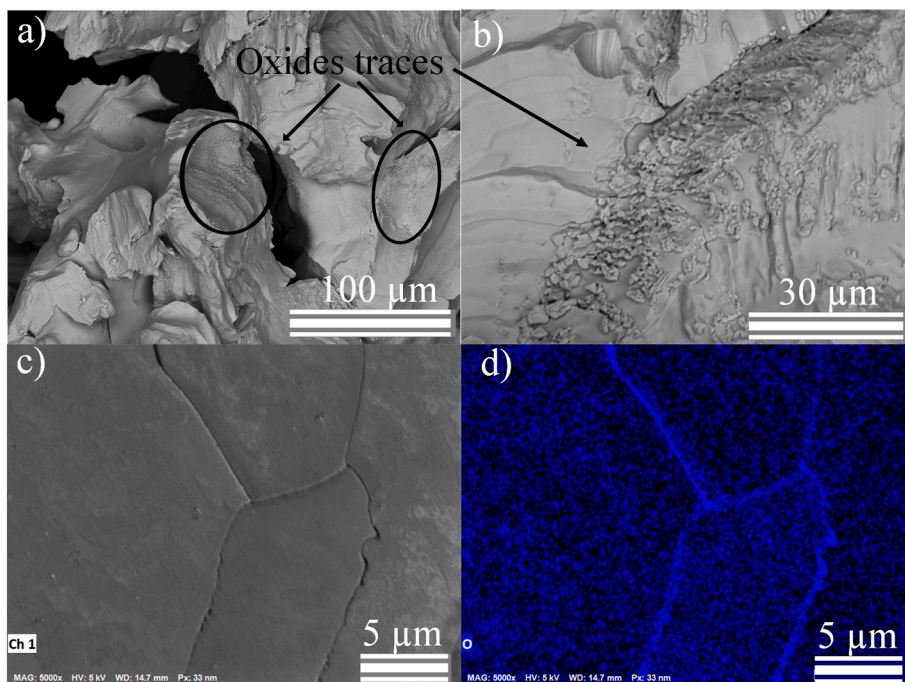


Fig. 9. C-60 parameter set: (a and b) SEM images of oxidation traces observed on the compressive fracture surface; (c) SEM image on the polished cross-section and (d) corresponding EDS map.

elements are plotted as functions of the h/t ratio in Fig. 11a and b. These evolutions can be compared to those of the grain size in the same figure. For a constant layer thickness, an increase in the h/t ratio means an increase in the hatching space and a smaller overlap of two subsequent laser tracks, and a lower inclination to trigger primary recrystallization. A smaller overlap will therefore correspond to a higher density of the LAGB substructure elements at the expense of a lower density of the HAGB structural elements (grains). To verify this point, a comparison was made between samples E-120 and C-60 having the same predicted melt pool widths ($W \approx 135 \mu\text{m}$), but for which the overlap ratio (W/h) goes from 1.1 (E-120) to 2.3 (C-60). As presented in Fig. 11c,d,e,f, sample E-120 with a smaller overlap manifests a higher LAGB density, a lower HAGB density and larger grains than sample C-60 with a greater overlap. Finally, for all the studied samples, grains are elongated ($C50g = [0.4; 0.55]$, $C90g = [0.65; 0.75]$) and oriented in the build direction, which is common for this process [34,40].

3.3. Mechanical testing

3.3.1. Room temperature testing

The mechanical properties (YS, UCS and δ) of all the tested samples are summarized in Table A.1 in the appendix. It must be noted that two types of mechanical behavior were observed during compression testing (Fig. 12a). Some of the samples broke under the maximum load, presenting “short” stress-strain diagrams with monotonically increasing stresses akin to conventional stress-strain diagrams for ductile materials. The associated fracture surface observed using SEM (Fig. 12b) is relatively clean, without impurities, and shows standard ductile convection fracture marks. The others, “long” stress-strain diagrams, demonstrate two inflection points, the first accompanied by audible cracking far before reaching the second inflection point, corresponding to the maximum stress before failure. These last samples (VED-BR sets A, B and D) can be distinguished by their lower values of printed densities ($\leq 92\%$) and yield strengths ($\leq 250 \text{ MPa}$). This two-stage behavior is attributed to the presence of unmelted particles inside the pores which are crushed and deformed along the compression test, as seen in the SEM image of the fracture surface of sample B-60 (Fig. 12c). Since this behavior is related to

the presence in the specimens of a significant number of process-induced flaws (pores, unmelted particles inside the pores and micro-cracks), the A, B and D parameter sets are excluded from further analyses.

Note furthermore that the mechanical properties of the remaining C and E sets follow the same trend as the printed densities (Fig. 13 vs Fig. 7b). Indeed, with the increase of h/t , the strength first increases to reach a maximum at $h/t = 2$, then decreases to $h/t = 3.3$ and finally increases again. When comparing the room-temperature mechanical properties of samples with the highest measured densities, C-60 and E-120, the mechanical properties of the former appear to be significantly higher than those of the latter: +21 % for UCS, +12 % for YS and +35 % for strain under maximum load (not shown in Fig. 13). This is consistent with a finer grain structure of the C-60 samples as compared to their E-120 counterparts (~ 100 vs $\sim 125 \mu\text{m}$) (Fig. 11c). The C-60 parameter set ($P = 179 \text{ W}$, $v = 133 \text{ mm/s}$, $h = 60 \mu\text{m}$) is therefore considered as an optimized set of printing parameters and retained for subsequent study.

3.3.2. Elevated temperature testing

Using the C-60 set of printing parameters, selected using density measurements and mechanical testing at room temperature, new specimens were printed and tested at 600, 800 and 1000 °C. It must be noted that while the argon-filled atmosphere was sufficient to prevent oxidation at 600 °C, specimens suffered non-negligible oxidation during testing at 800 and 1000 °C. A thick white smoke was observed outside the compression chamber and samples were found covered with a shiny white lamina (Fig. 14a) at the end of testing. The estimated mass loss corresponded to $8.6 \pm 2.7\%$ at 800 °C and $9.4 \pm 0.8\%$ at 1000 °C. XRD analyses of the thermocouple-instrumented specimen (Fig. 14b) before and after the thermal cycling revealed that this phenomenon corresponds to the formation and vaporization of MoO_3 oxides, which were not initially present in the sample. (Note that the reported values of YS, UCS and δ obtained at 800 and 1000 °C were not adjusted to compensate for this mass loss.)

Fig. 15 presents the stress-strain diagrams obtained at 20, 600, 800 and 1000 °C. Globally, the higher the testing temperature, the lower the strength characteristics (YS, UCS), and the higher the strain under maximum load, but this evolution is not monotonic (Table 4).

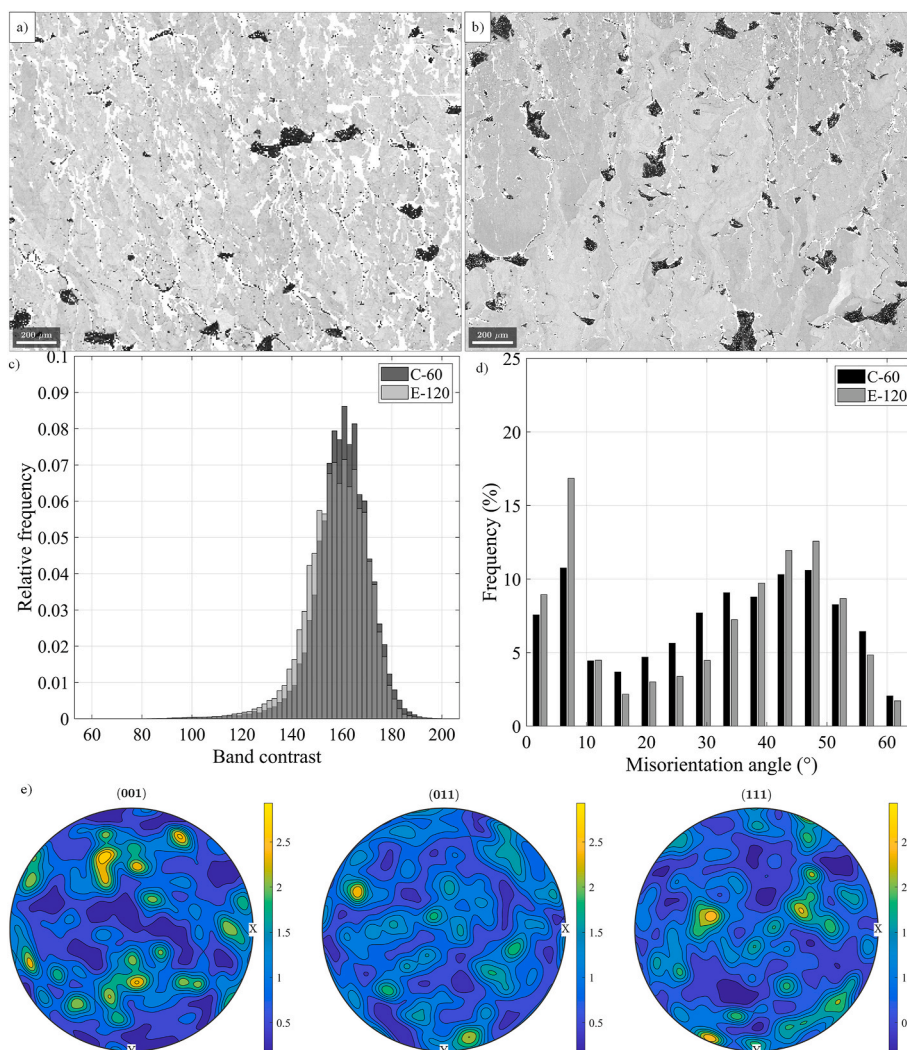


Fig. 10. Band contrast (BC) diagrams of samples a) C-60 and b) E-120; c) BC cumulative histograms and d) MacKenzie plots of samples C-60 and E-120; e) pole figures of sample C-60.

3.4. Printability

To assess the printability limits of the parameter set selected (C-60), geometric attributes of some selected geometric features were measured. A stitched image of the wall artifact is presented in Fig. 16a along with the methodology used to measure the wall thickness on top of the parts (Fig. 16b). Regarding the wall features, all the thicknesses were successfully printed. Their measured dimensions were compared to the nominal values and subjected to a linear regression analysis in Fig. 16c. The direction coefficient was close to 1 (1.08), $R_{adj}^2 = 0.99$ and $RMSE = 0.063$, with no pattern in the residuals.

For the gaps, the narrowest of them (0.1 and 0.2 mm) were not printed. For the 0.1 mm gap, since no offset was applied, two neighboring melt tracks overlapped (considering the melt pool width predicted with the model of $\sim 140 \mu\text{m}$). For the nominal sizes of 0.1 and 0.2 mm, the empty space between two neighboring tracks was commensurate with the diameter of powder particles. For wider gaps, the linear regression analysis (Fig. 16d) gave a direction coefficient close to 1 (1.02), $R_{adj}^2 = 0.99$ and $RMSE = 0.041$, with no pattern in the residuals. Note that particles attached to the surface induced significant deviations from the nominal values (Fig. 16d). Regarding the gyroids structures, they were subjected to ultrasonic cleaning, and their porosity estimated using the Archimedes method provided an excellent correspondence with the nominal values, 50 and 59 % versus 50 and 60 %, respectively.

4. Discussion

4.1. Printed density: prediction versus experiment

This study showed the complexity of interactions between the process parameters and printed density. Indeed, if it is commonly accepted that *VED* is a reliable metric to quantify the LPBF process conditions, this study demonstrated that *VED* alone is not sufficient and must rather be used in combination with the *BR* and *h/t* indicators to find the absolute values of printing parameters P , v , h and t . This highlights the usefulness of using numerical models for the rough assessment of printed density as a function of process parameters, thus reducing the often too costly and time-consuming plans of experiments. However, this work revealed a significant discrepancy between the predicted printed densities and their experimentally measured equivalents. While the predicted values show a clear optimum at $h/t = 2.5$ (Fig. 7a), the experimentally observed trends are much more complicated and indicate two optimal regions at $h/t = 2$ and $h/t = 4$ (Fig. 7b).

Such an irregular evolution of printed density as a function of the process parameters was also observed by Higashi et al. [40], in their study on pure molybdenum fabricated by LPBF. While the authors did not provide explanations for such discontinuities, it appears that a non-monotonic decrease in printed porosity observed in their study was accompanied by drastic changes in both the nature of process-induced

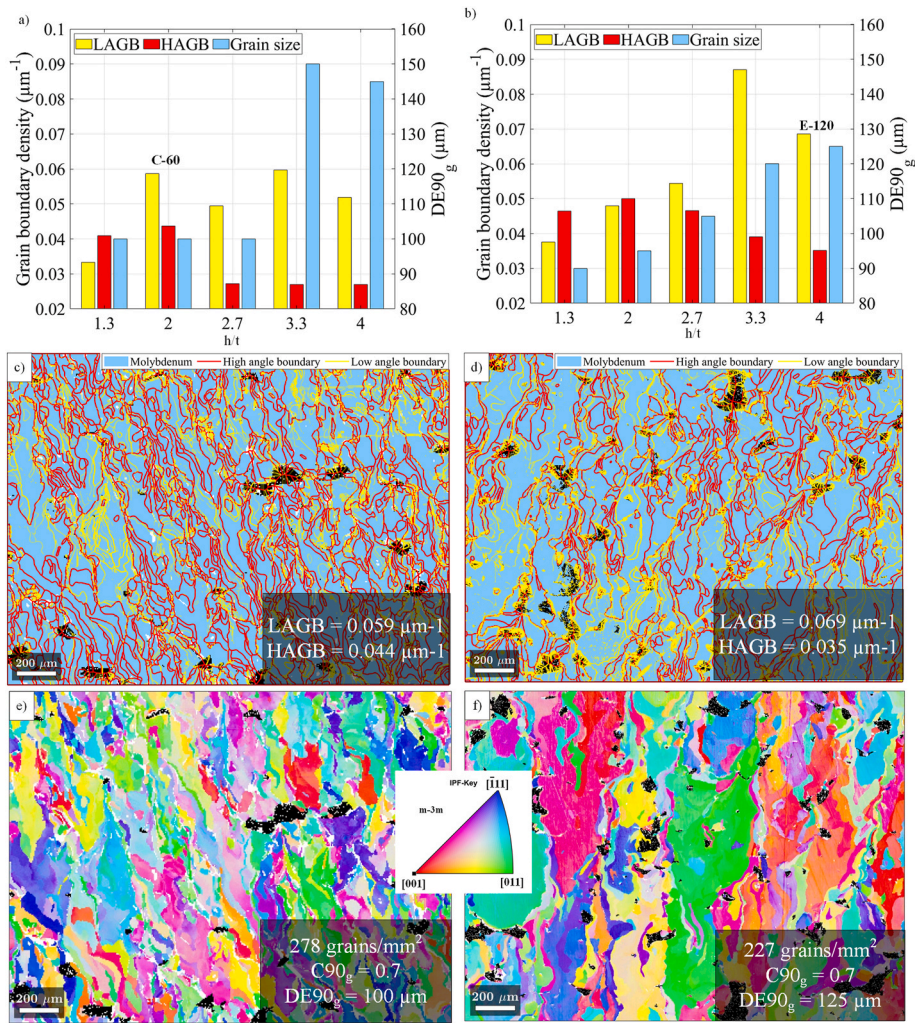


Fig. 11. LAGB, HAGB densities and grain size (DE90_g) as functions of the h/t ratio for the VED-BR set C (a) and E (b); phase maps highlighting LAGB (yellow) and HAGB (red) for the specimens C-60 (c) and E-120 (d); orientation maps (IPF Y) for the specimens C-60 (e) and E-120 (f). (For interpretation of the references to color in this figure legend, the reader is referred to the Web version of this article.)

flaws (small spherical gas-filled pores replaced the elongated lack-of-fusion defects) and the crystallographic texture ($\langle 110 \rangle$ replaced $\langle 001 \rangle$). In our study, no significant texture modifications were observed, but the highest printed density cases C-60 and E-120 also presented the largest fractions of small spherical gas-filled pores ($DE < 50 \mu\text{m}$ and $C > 0.7$) as compared to the other printing regimes.

It can be asserted that the printed density prediction model used in this study, which is merely a correlation between the calculated melt pool dimensions and the density calibration function (Fig. 3c), was not meant to consider the complex physical phenomena impacting the final density of printed parts. It was used to establish a sound experimental plan of this work, thus avoiding the trial-and-error approach.

Since the objective of this study was to maximize the printed density and mechanical properties of as-built molybdenum specimens, Fig. 17 compares the results obtained herein for $h/t = 2$ with those from the literature [38,40,41,48]. Only authors who measured their density using the image analysis were retained. According to this representation, the highest printed densities were obtained in the 200–400 J/mm^3 VED range and in the 2–5 cm^3/h BR range. However, with the parameter sets corresponding to these conditions, all the authors reported the presence of microcracks. Conversely, the VED values used in this study were higher ($>400 \text{ J}/\text{mm}^3$), while the BR values were lower ($<1.63 \text{ cm}^3/\text{h}$) than those in the literature, thus resulting in lower cooling rates. It can therefore be hypothesized that the appearance of microcracks in the

previously cited works can be explained by excessively high cooling rates occurring during the process.

Faidel et al. [38] performed experiments in the VED-BR range which is the closest to the one used in this study and with a similar printer ($P_{\text{max}} = 200 \text{ W}$). They reported printed densities ranging between 49 and 78 % (Fig. 17), which are much lower than those obtained in this study. Such a significant decrease in printed density can be explained by the use of a suboptimal $h/t \leq 1$. In fact, to be in the similar BR range, while using such a narrow hatching space, the authors of the referenced study were obliged to switch to higher scanning speeds (up to 4000 mm/s), thus generating smaller melt pools and potentially unstable melting conditions, resulting in highly porous parts. According to the observations above, the VED-BR range leading to high-density crack-free printing of molybdenum corresponds to a combination of high VED (400–1200 J/mm^3), reduced BR (0.5–2 cm^3/h), and optimized $h/t \approx 2$.

4.2. Microstructure evolution

Considering printing with the C VED-BR set (see Table A.1 in the appendix), the laser power was fixed at 180 W, the hatching space increased from 40 to 120 μm and the scanning speed decreased from 199 to 66 mm/s. In the case of a single-track fusion, this decrease in the scanning speed must correspond to an increase in the linear laser energy density ($LED = P/v$) from 0.9 to 2.7 J/mm , an increase in the melt pool

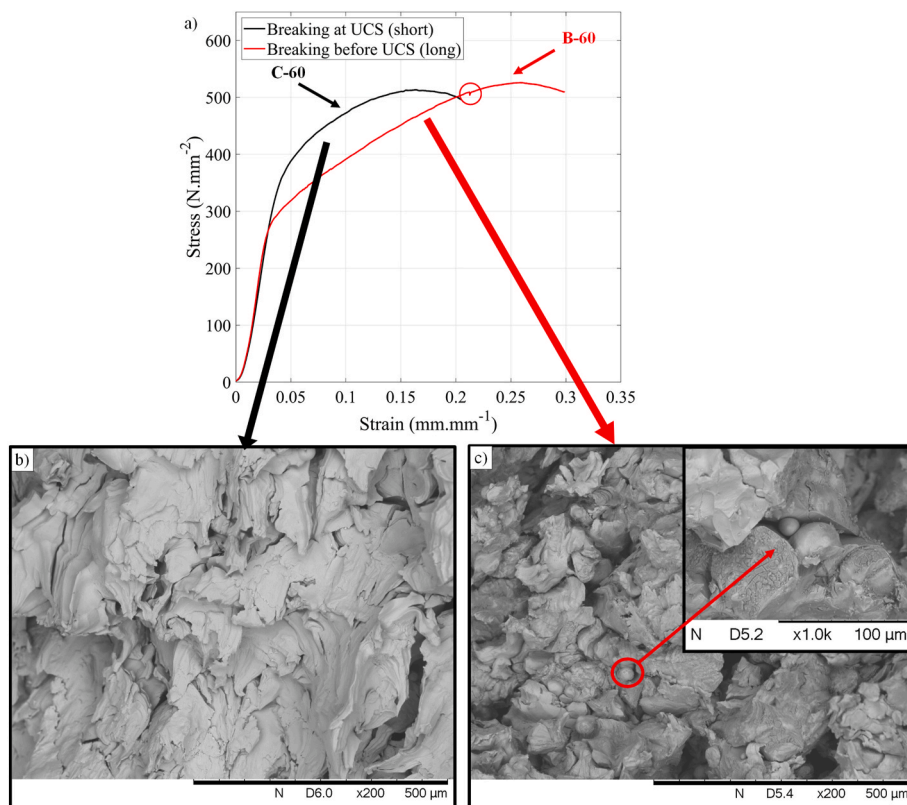


Fig. 12. a) Stress-strain diagrams of the C-60 and B-60 samples highlighting two distinct behaviors observed during the compression tests; SEM images of the fracture surfaces of samples b) B-60 and c) C-60.

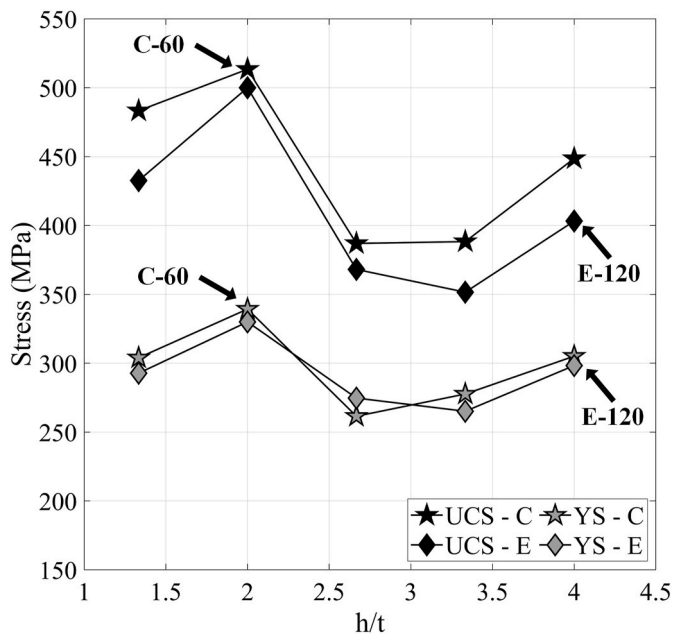


Fig. 13. YS and UCS for C and E process parameter sets; arrows point to the C-60 and E-120 specimens with the highest printed densities.

size, decrease in the cooling rate and increase in the crystallized grains size, according to the welding analogy in Ref. [62]. In the case of a multi-track fusion however, when the hatching space increased from 40 to 120 μm , the distance between two neighboring tracks and therefore the heat affected zone, become larger, thus additionally contributing to the microstructure coarsening (see an increase in the grain size from 100

to 150 μm , Fig. 11a). For the lower h/t ratios (h decreases), a second competitive phenomenon associated with an increase in the melt pool overlapping ratio (W/h) occurs, and triggers complex crystallization/recrystallization phenomena leading to the small grain formation (LAGB density decreases and HAGB density increases (Fig. 11a)). The formation of such small grains was also reported in the study using double laser exposure [37].

Similar conclusions can be made for the specimens printed using the VED-BR set E. The C-60 and E-120 parameters sets resulting in the highest printed density of this study ($\sim 97\%$) provide the same linear energy densities of 1.35 J/mm. However, the former case implies a greater overlapping of two neighboring tracks and consequently, a narrower heat affected zone and potentially a greater recrystallization potential, leading at the end, to an overall finer microstructure (100 μm for C-60 as compared to 125 μm for E-120, Fig. 11a and b).

Although the columnar aspect of a grain structure in LPBF molybdenum is sufficiently addressed in the literature [34,40,43], the printing strategy to obtain a refined and equiaxed microstructure is not clear-cut, and is highly dependent on the characteristics of a printer used. Wang et al. [43], highlighted changes in the grain morphology caused by different scanning strategies, while Higashi et al. [40], using a 400 W printer, observed significant variations in the crystallographic texture and grain size, depending on the process parameters. Their observations, coupled with the results of this study, demonstrate the complexity of the crystallization/recrystallization phenomena occurring during LPBF of molybdenum. To circumvent this complexity while trying to refine the printed microstructure, some authors, such as Kaserer et al. [63], have put forth a completely different strategy, using alloying with other elements, such as carbon (C).

4.3. Mechanical properties

The room temperature mechanical properties obtained in this study

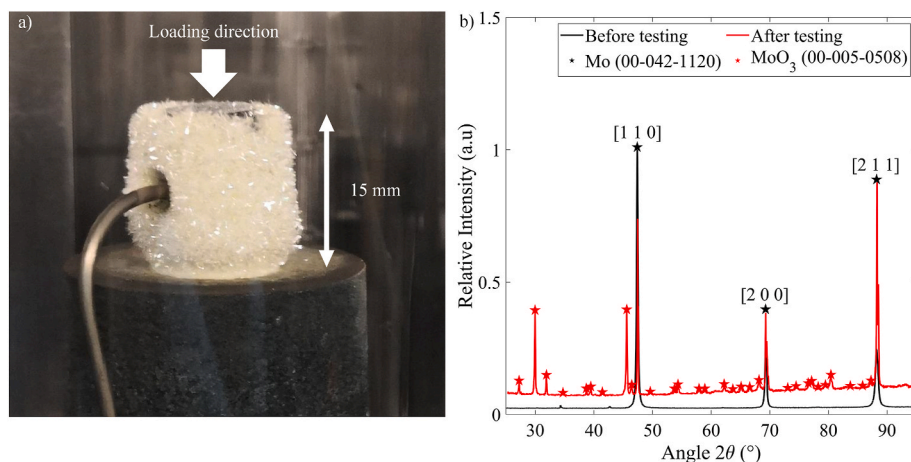


Fig. 14. Thermocouple-instrumented sample: a) Photo with the oxide layer; b) XRD before and after the temperature cycling (without load).

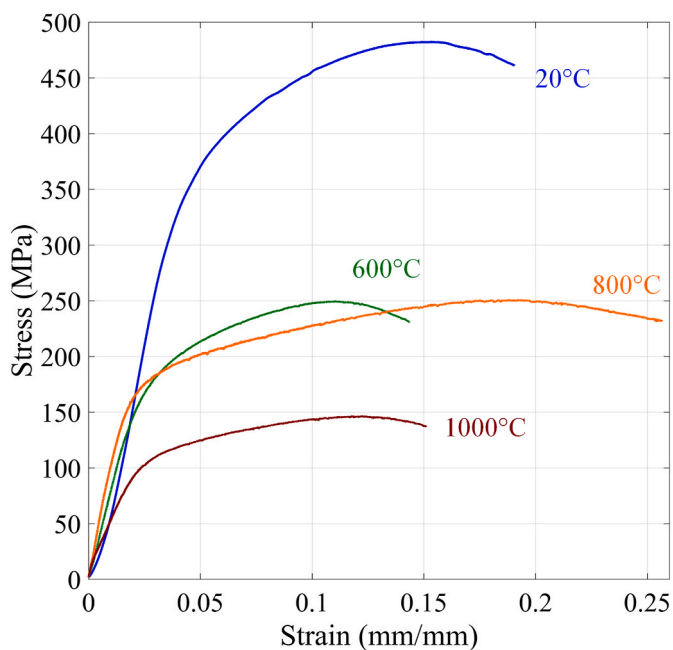


Fig. 15. Representative stress-strain compression diagrams (C-60) at 20, 600, 800 and 1000 °C.

Table 4
Mechanical properties in compression at room and elevated temperatures.

Testing temp., °C	YS, MPa	UCS, MPa	δ , %
20	340 ± 20	500 ± 15	11 ± 1
600	150 ± 20	240 ± 30	8 ± 1
800	160 ± 5	260 ± 8	14 ± 1
1000	90 ± 10	150 ± 18	9 ± 4

were first compared to an industrial standard B387-18 [64] for vacuum arc-cast and powder metallurgy molybdenum and molybdenum alloy bars, rods and wires (see Fig. 18). This standard could be considered as a potential target for printed molybdenum. The mechanical properties at elevated temperatures obtained in this study were also compared with the literature [3,5,65,66] as shown in Fig. 18 for the ultimate strength. Note that the referenced authors performed tension testing and reported significant oxidation during high temperature testing.

Regarding our experiments, they were carried out in compression and the measured weight variations are consistent with the expected

oxidation kinetics for molybdenum [67]. At 600 °C, samples are supposed to undergo linear oxidation with low kinetics ($k \approx 3.4 \cdot 10^{-4} \text{ mg}/(\text{cm}^2 \cdot \text{s})$). The overall duration of these tests was too short (<2h) for such small weight gains to be detected. However, at higher temperatures, competitive oxidation and volatilization occurred, and at over 700 °C, the volatilization of MoO_3 became predominant, leading to linear weight loss kinetics ($k \approx -1.2 \cdot 10^{-2} \text{ mg}/(\text{cm}^2 \cdot \text{s})$). The theoretical kinetic rates are consistent with our observations (Fig. 14a) and measurements.

Regarding the strength characteristics, compared to other LPBF-produced specimens [3], the values obtained in this study are either higher (room temperature) or comparable (600 °C), despite significantly lower printed densities: 97 % in this study as compared to 99.5 % in the referenced work. One of the explanations for this discrepancy is the difference in testing modes (compression versus tension). Indeed, the presence of cracks is theoretically more critical in tension than in compression, which can explain higher mechanical resistance at room temperature of the specimens of this study. As far as the high temperature testing is concerned, this difference in testing modes becomes negligible compared to the degradation induced by the concomitant oxidation.

As compared to the EB-PBF molybdenum [65], the specimens of this study exhibit from 15 to 30 % lower mechanical resistance at both room temperature and in the 700–750 °C temperature range: 570 MPa (RT) and 320 MPa (700–750 °C) for the former as compared to 500 MPa (RT) and 250 MPa (800 °C) for the latter. This discrepancy can be attributed to much higher printed densities of the EB-PBF specimens as compared to the specimens of this study: >99.5 % in the latter as compared to 96.5 % in the former, and a more favorable as-printed texture (mixed (001)/(111)-fiber grains). Furthermore, with EB-PBF using a vacuum atmosphere, the final oxygen content measured in produced parts is generally much lower than within LPBF parts. With EB-PBF, the literature reports 100 ppm or even lower level of oxygen [68], while with the LPBF process, the values are rather in the 400–2000 ppm range [34,69,39]. Consequently, oxygen segregation at the grain boundaries reported in the literature is more probable during LPBF, leading to a greater embrittlement and lower mechanical properties of the LPBF molybdenum as compared to its EB-PBF counterpart.

Finally, compared to the conventional PM processes, the results obtained in this study are very similar across the entire temperature range. The non-monotonic decrease of mechanical properties around 800 °C observed in this study was also encountered by Carreker and Guard [66]. They related this phenomenon to a manifestation of strain aging caused by the presence of impurities in body-centered cubic (BCC) metals. This theory was first proposed and well-studied by Cottrell [70], who attributed discontinuous yielding in these metals to the pinning of dislocations by impurities or interstitial atoms. These observations are also

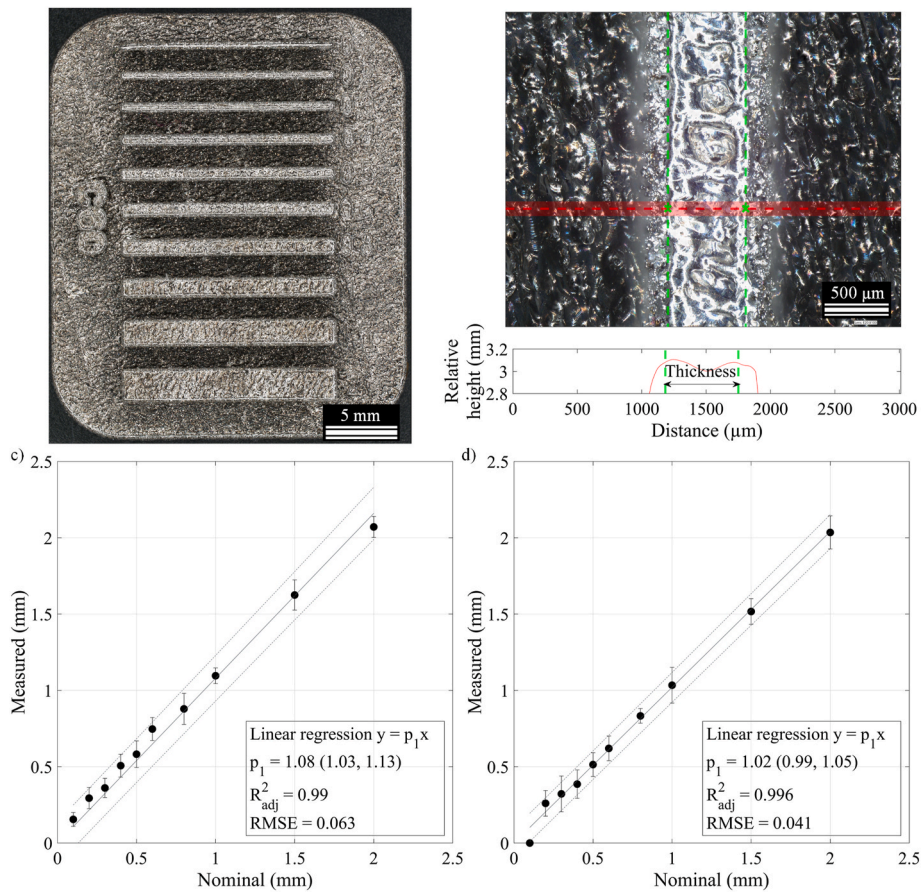


Fig. 16. a) Optical microscopy observations of walls; b) measurement of its top thickness using the height profile line represented in red; c) linear regressions between the nominal and the microscope-measured thickness of (c) walls and (d) gaps, with the confidence interval at 95 % margins. (For interpretation of the references to color in this figure legend, the reader is referred to the Web version of this article.)

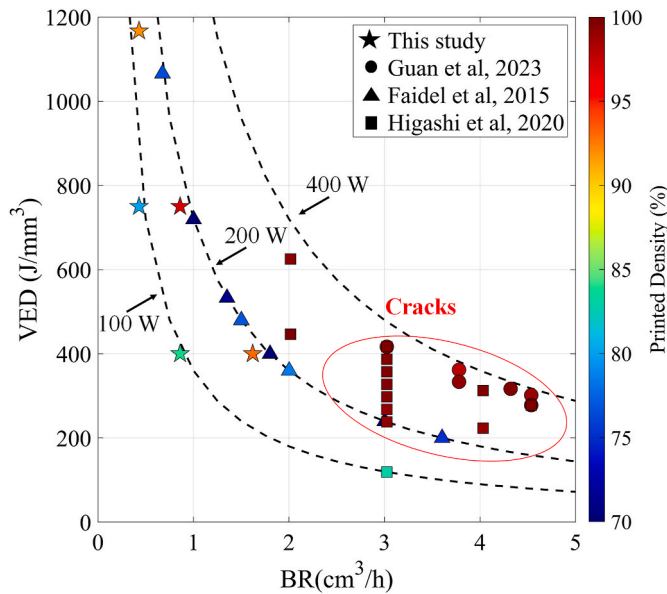


Fig. 17. a) Image-measured printed density in the VED-BR plan for this study ($h/t = 2$) and the current literature [38,40,41,48]; red ellipse indicates zone corresponding to microcracks. Dashed lines delimit the frontier of 100, 200 and 400W printers' boundaries. (For interpretation of the references to color in this figure legend, the reader is referred to the Web version of this article.)

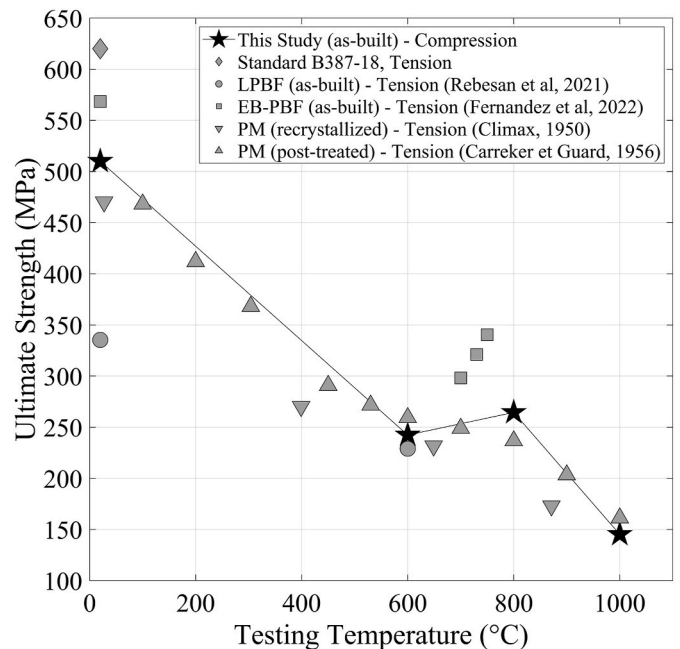


Fig. 18. Evolution of the Ultimate Strength depending on the mechanical testing temperature. Comparison is made to the standard B387-18 [64] and the literature [3,5,65,66]; Note that the strength values of this study was obtained in compression, while those from the literature were obtained in tension.

in qualitative agreement with those of Tury and Krauz [71] on molybdenum containing nitrogen impurities. Of note, maximum values of strain to failure of pure molybdenum products found in the literature vary significantly: from <2 % for the LPBF Mo specimens in Ref. [3] to ~ 60 % for the recrystallized press-sintered specimens in Ref. [5], thus preventing any comparisons with the results of this study.

It is recommended that for high temperature applications, refractory metals, such as molybdenum, should be used in fully recrystallized condition [72]. If the mechanical properties of the as-built specimens of this study appear to be competitive compared to the traditional processes, at high temperatures and after long term exposure, the typical anisotropic microstructure associated with the LPBF process may evolve towards a coarser and equiaxed microstructure, thus negatively affecting the mechanical properties at room temperature. Consequently, depending on the objectives (targeting either room or high temperature applications), different post-treatments can be considered.

In the literature, basic post-treatments such as stress relief (980 °C for 2h) or annealing (1170 °C for 12h) are reported to be highly ineffective in modifying the microstructure and influence the mechanical properties of molybdenum [73]. To transform the microstructure of LPBF tungsten parts, Shi et al. [74] tried to apply HIP treatments with at 1400 and 1600 °C ($P = 150$ MPa for 2h). According to them, only HIP at the highest temperature of their study (1600 °C) was sufficient to trigger the recrystallization process. Consequently, to improve the isotropy of mechanical properties of the LPBF refractory metals, they must be post-treated at extremely high temperatures, which represents an additional technological challenge. An alternative solution could be to add alloying elements in the feedstock material with the objective of improving its printing behavior, reducing oxidation and refining the microstructure during the process.

5. Conclusions

A numerical model previously developed for the melt pool predictions with tungsten powders was used to build a plan of experiments of this study. Structural analyses and mechanical testing at room temperature revealed a strong link between the physical and mechanical

properties of the printed specimens and the process parameters, leading to the selection of an optimal set of printing parameters ($P = 179$ W, $v = 133$ mm/s, $h = 60$ μ m and $t = 30$ μ m). This enables to produce crack-free specimens with a printed density of 97 %, UCS = 510 MPa, YS = 340 MPa and $\delta = 11$ % at room temperature. This same set of parameters was then proven to be effective to obtain competitive mechanical properties at elevated temperatures and provide a sufficient resolution to build geometric artifacts, such as walls, gaps and lattice structures.

According to the results obtained, the possibilities to print high density molybdenum parts with low-power printers appear limited, since the optimal set of printing parameters obtained in the framework of this study are close to the technical limits of the equipment.

CRediT authorship contribution statement

Aurore Leclercq: Writing – original draft, Visualization, Validation, Software, Methodology, Investigation, Formal analysis, Data curation, Conceptualization. **Thibault Mouret:** Writing – original draft, Visualization, Software, Methodology, Investigation, Formal analysis, Data curation. **Vladimir Brailovski:** Writing – review & editing, Visualization, Validation, Supervision, Resources, Project administration, Methodology, Funding acquisition, Conceptualization.

Declaration of competing interest

The authors declare that they have no known competing financial interests or personal relationships that could have appeared to influence the work reported in this paper.

Acknowledgments

The authors acknowledge the financial support provided by PRIMA Québec (Pôle de recherche et d'innovation en matériaux avancés) in the framework of the M-ERA.NET program, NSERC (Natural Sciences and Engineering Research Council of Canada) and PyroGenesis Canada Inc.

Appendix

Table A.1

Printed specimens: nomenclature, plan of experiments, predicted density, measured density, error between the densities, yield strength at 0.2 % offset, ultimate compression strength and strain under maximum load.

Name	Hatching Space (μ m)	Power (W)	Speed (mm/s)	Volumetric Energy Density (J/mm^3)	Build Rate (cm^3/h)	Predicted Density (%)	Image Analysis Density (%)	Absolute Error between Densities (%)	YS at 0.2 % (MPa)	UCS (MPa)	Strain under Maximum Load (%)
A-40	40	140	100	1167	0.43	94	94	0	230	380	11
B-40		90	100	750	0.43	91	87	4	220	510	21
C-40		179	199	750	0.86	95	89	6	300	480	11
D-40		96	199	400	0.86	93	84	11	250	490	19
E-40		180	375	400	1.62	95	90	6	290	430	9
A-60	60	140	67	1167	0.43	98	92	7	280	550	17
B-60		90	66	750	0.43	94	80	18	240	550	23
C-60		179	133	750	0.86	98	96	2	340	510	11
D-60		96	133	400	0.86	94	84	11	270	530	21
E-60		180	250	400	1.62	98	93	5	330	500	11
A-80	80	140	50	1167	0.43	98	94	5	240	430	14
B-80		90	50	750	0.43	96	90	6	200	430	20
C-80		179	100	750	0.86	99	96	3	260	390	9
D-80		96	100	400	0.86	96	89	8	190	360	15
E-80		180	188	400	1.62	98	95	3	280	370	7
A-100	100	140	40	1167	0.43	98	94	4	240	430	14
B-100		90	40	750	0.43	95	92	4	200	410	18
C-100		179	80	750	0.86	98	95	4	280	390	8
D-100		96	80	400	0.86	95	91	5	200	380	15

(continued on next page)

Table A.1 (continued)

Name	Hatching Space (μm)	Power (W)	Speed (mm/s)	Volumetric Energy Density (J/mm^3)	Build Rate (cm^3/h)	Predicted Density (%)	Image Analysis Density (%)	Absolute Error between Densities (%)	YS at 0.2 % (MPa)	UCS (MPa)	Strain under Maximum Load (%)
E-100		180	150	400	1.62	98	94	5	270	350	6
A-120	120	140	33	1167	0.43	96	93	3	240	430	14
B-120		90	33	750	0.43	95	91	3	180	400	19
C-120		179	66	750	0.86	98	95	3	300	450	11
D-120		96	66	400	0.86	95	89	6	220	390	11
E-120		180	125	400	1.62	97	96	1	300	400	7

Data availability

Data are contained within the article.

References

- [1] P. Hidnert, W.B. Gero, Thermal expansion of molybdenum, *Sci. Pap. Bur. Stand.* 19 (1924) 429, <https://doi.org/10.6028/nbsciapaper.171>.
- [2] R.D. Allen, L.F. Glasier, P.L. Jordan, Spectral emissivity, total emissivity, and thermal conductivity of molybdenum, tantalum, and tungsten above 2300°K, *J. Appl. Phys.* 31 (1960) 1382–1387, <https://doi.org/10.1063/1.1735847>.
- [3] P. Rebesan, M. Ballan, M. Bonesso, A. Campagnolo, S. Corradetti, R. Dima, C. Gennari, G.A. Longo, S. Mancin, M. Manzolaro, G. Meneghetti, A. Pepato, E. Visconti, M. Vedani, Pure molybdenum manufactured by Laser Powder Bed Fusion: thermal and mechanical characterization at room and high temperature, *Addit. Manuf.* 47 (2021) 102277, <https://doi.org/10.1016/j.addma.2021.102277>.
- [4] H. Baker, Properties of metals, in: J.R. Davis (Ed.), *Met. Handb.*, Desk Ed., second ed., ASM International, 1998, pp. 114–121, <https://doi.org/10.31399/asm.hb.mhde2.a0003086>.
- [5] Climax Molybdenum Company of Michigan, *Fourth Annual Report - Arc-Cast Molybdenum-Base Alloys*, 1950.
- [6] C.A. Hampel, Corrosion properties of tantalum, columbium, molybdenum and tungsten, *Corrosion* 14 (1958) 29–32, <https://doi.org/10.5006/0010-9312-14.12.29>.
- [7] W.A. Badawy, F.M. Al-Kharafi, Corrosion and passivation behaviors of molybdenum in aqueous solutions of different pH, *Electrochim. Acta* 44 (1998) 693–702, [https://doi.org/10.1016/S0013-4686\(98\)00180-7](https://doi.org/10.1016/S0013-4686(98)00180-7).
- [8] W. Cairang, T. Li, D. Xue, H. Yang, P. Cheng, C. Chen, Y. Sun, Y. Zeng, X. Ding, J. Sun, Enhancement of the corrosion resistance of Molybdenum by La_2O_3 dispersion, *Corros. Sci.* 186 (2021) 109469, <https://doi.org/10.1016/j.corsci.2021.109469>.
- [9] K. Shree Meenakshi, S. Ananda Kumar, Corrosion resistant behaviour of titanium – molybdenum alloy in sulphuric acid environment, *Mater. Today Proc.* 65 (2022) 3282–3287, <https://doi.org/10.1016/j.matpr.2022.05.389>.
- [10] H. Zhao, L. Xie, C. Xin, N. Li, B. Zhao, L. Li, Effect of molybdenum content on corrosion resistance and corrosion behavior of Ti-Mo titanium alloy in hydrochloric acid, *Mater. Today Commun.* 34 (2023) 105032, <https://doi.org/10.1016/j.mtcomm.2022.105032>.
- [11] C. Fernandes, I. Taurino, Biodegradable molybdenum (Mo) and tungsten (W) devices: one step closer towards fully-transient biomedical implants, *Sensors* 22 (2022) 3062, <https://doi.org/10.3390/s22083062>.
- [12] A. Toschka, G. Pöhle, P. Quadbeck, C.V. Suschek, A. Strauß, C. Redlich, M. Rana, Molybdenum as a potential biocompatible and resorbable material for osteosynthesis in craniomaxillofacial surgery—an in vitro study, *Int. J. Mol. Sci.* 23 (2022) 15710, <https://doi.org/10.3390/ijms232415710>.
- [13] A.K. Aboul-Gheit, A.E. Awadallah, S.M. Abdel-Hamid, A.A. Aboul-Enein, D.S. El-Desouki, Direct conversion of natural gas to petrochemicals using monofunctional Mo/SiO₂ and H-ZSM-5 zeolite catalysts and bifunctional Mo/H-ZSM-5 zeolite catalyst, *Petrol. Sci. Technol.* 30 (2012) 893–903, <https://doi.org/10.1080/10916466.2010.493912>.
- [14] C.J.A. Mota, Valter L.C. Gonçalves, J.E. Mellizo, A.M. Rocco, J.C. Fadigas, R. Gambetta, Green propene through the selective hydrogenolysis of glycerol over supported iron-molybdenum catalyst: the original history, *J. Mol. Catal. Chem.* 422 (2016) 158–164, <https://doi.org/10.1016/j.molcata.2015.11.014>.
- [15] Plansee | Des métaux solides pour des produits solides | Plansee, (n.d.). <https://www.plansee.com/www.plansee.com/fr.html> (accessed October 5, 2023).
- [16] J.R. Davis, *Metals Handbook*, desk edition, second ed., ASM International, Materials Park, Ohio, 1998.
- [17] H.L. Moody, D.H. Smith, R.L. Haddock, S.S. Dunn, Tungsten and molybdenum ablation modeling for Re-entry applications, *J. Spacecraft Rockets* 13 (1976) 746–753, <https://doi.org/10.2514/3.57136>.
- [18] J. Wadsworth, T.G. Nieh, J.J. Stephens, Recent advances in aerospace refractory metal alloys, *Int. Mater. Rev.* 33 (1988) 131–150, <https://doi.org/10.1179/imr.1988.33.1.131>.
- [19] N. Iqbal, A. Afzal, I. Khan, M.S. Khan, A. Qurashi, Molybdenum impregnated g-C₃N₄ nanotubes as potentially active photocatalyst for renewable energy applications, *Sci. Rep.* 11 (2021) 16886, <https://doi.org/10.1038/s41598-021-96490-6>.
- [20] A. Santagata, M.L. Pace, A. Bellucci, M. Mastellone, E. Bolli, V. Valentini, S. Orlando, E. Sani, S. Failla, D. Sciti, D.M. Trucchi, Enhanced and selective absorption of molybdenum nanostructured surfaces for concentrated solar energy applications, *Materials* 15 (2022) 8333, <https://doi.org/10.3390/ma15238333>.
- [21] L.B. Luntberg, *A Critical Evaluation of Molybdenum and its Alloys for Use in Space Reactor Core Heat Pipes*, Los Alamos Scientific Laboratory, 1981.
- [22] B. Cheng, Y.-J. Kim, P. Chou, Improving accident tolerance of nuclear fuel with coated Mo-alloy cladding, *Nucl. Eng. Technol.* 48 (2016) 16–25, <https://doi.org/10.1016/j.net.2015.12.003>.
- [23] Z. Duan, H. Yang, Y. Satoh, K. Murakami, S. Kano, Z. Zhao, J. Shen, H. Abe, Current status of materials development of nuclear fuel cladding tubes for light water reactors, *Nucl. Eng. Des.* 316 (2017) 131–150, <https://doi.org/10.1016/j.nucengdes.2017.02.031>.
- [24] A.N. Shmelev, B.K. Kozhahmet, Use of molybdenum as a structural material of fuel elements for improving the safety of nuclear reactors, *J. Phys. Conf. Ser.* 781 (2017) 012022, <https://doi.org/10.1088/1742-6596/781/1/012022>.
- [25] B. Tabernig, N. Reheis, Joining of molybdenum and its application, *Int. J. Refract. Met. Hard Mater.* 28 (2010) 728–733, <https://doi.org/10.1016/j.jirmhm.2010.06.008>.
- [26] M. Schneider, L. Šimůnková, A. Michaelis, W. Hoogsteen, Electrochemical machining of molybdenum, *Int. J. Refract. Met. Hard Mater.* 101 (2021) 105689, <https://doi.org/10.1016/j.jirmhm.2021.105689>.
- [27] A. Taligani, R. Seede, A. Whitt, S. Zheng, J. Ye, I. Karaman, M.M. Kirka, Y. Katoh, Y.M. Wang, A review on additive manufacturing of refractory tungsten and tungsten alloys, *Addit. Manuf.* 58 (2022) 103009, <https://doi.org/10.1016/j.addma.2022.103009>.
- [28] B. Liu, P. Zhang, H. Yan, Q. Lu, H. Shi, Z. Liu, D. Wu, T. Sun, R. Li, Q. Wang, A review on manufacturing pure refractory metals by selective laser melting, *J. Mater. Eng. Perform.* (2024), <https://doi.org/10.1007/s11665-024-09693-z>.
- [29] A. Garcia-Colomo, D. Wood, F. Martina, S.W. Williams, A comparison framework to support the selection of the best additive manufacturing process for specific aerospace applications, *Int. J. Rapid Manuf.* 9 (2020) 194–211, <https://doi.org/10.1504/IJRAPIDM.2020.107736>.
- [30] P. Gradl, D.C. Tinker, A. Park, O.R. Mireles, M. Garcia, R. Wilkerson, C. McKinney, Robust metal additive manufacturing process selection and development for aerospace components, *J. Mater. Eng. Perform.* 31 (2022) 6013–6044, <https://doi.org/10.1007/s11665-022-06850-0>.
- [31] C. Song, Z. Deng, Z. Zou, L. Liu, K. Xu, Y. Yang, Pure tantalum manufactured by laser powder bed fusion: influence of scanning speed on the evolution of microstructure and mechanical properties, *Int. J. Refract. Met. Hard Mater.* 107 (2022) 105882, <https://doi.org/10.1016/j.jirmhm.2022.105882>.
- [32] M. Liu, J. Zhang, C. Chen, Z. Geng, Y. Wu, D. Li, T. Zhang, Y. Guo, Additive manufacturing of pure niobium by laser powder bed fusion: microstructure, mechanical behavior and oxygen assisted embrittlement, *Mater. Sci. Eng., A* 866 (2023) 144691, <https://doi.org/10.1016/j.msea.2023.144691>.
- [33] A. Leclercq, V. Brailovski, Improving laser powder bed fusion printability of tungsten powders using simulation-driven process optimization algorithms, *Materials* 17 (2024) 1865, <https://doi.org/10.3390/ma17081865>.
- [34] J. Braun, L. Kaserer, J. Stajkovic, K.-H. Leitz, B. Tabernig, P. Singer, P. Leibenguth, C. Gspan, H. Kestler, G. Leichtfried, Molybdenum and tungsten manufactured by selective laser melting: analysis of defect structure and solidification mechanisms, *Int. J. Refract. Met. Hard Mater.* 84 (2019) 104999, <https://doi.org/10.1016/j.jirmhm.2019.104999>.
- [35] L. Yang, J. Yang, F. Han, Z. Zhang, Q. Li, Z. Dong, L. Wang, N. Ofori-Opoku, N. Provatat, Hot cracking susceptibility prediction from quantitative multi-phase field simulations with grain boundary effects, *Acta Mater.* 250 (2023) 118821, <https://doi.org/10.1016/j.actamat.2023.118821>.
- [36] H. Xing, P. Hu, J. Han, S. Li, S. Ge, X. Hua, B. Hu, F. Yang, K. Wang, P. Feng, Effects of oxygen on microstructure and evolution mechanism of body-centred-cubic molybdenum, *Int. J. Refract. Met. Hard Mater.* 103 (2022) 105747, <https://doi.org/10.1016/j.jirmhm.2021.105747>.
- [37] N. Alinejadian, P. Wang, L. Kollo, K.G. Prashanth, Selective laser melting of commercially pure molybdenum by laser rescanning, 3D print, *Addit. Manuf.* 10 (2023) 785–791, <https://doi.org/10.1089/3dp.2021.0265>.
- [38] D. Faidel, D. Jonas, G. Natour, W. Behr, Investigation of the selective laser melting process with molybdenum powder, *Addit. Manuf.* 8 (2015) 88–94, <https://doi.org/10.1016/j.addma.2015.09.002>.
- [39] N.E. Ellsworth, R.A. Kemnitz, C.C. Eckley, B.M. Sexton, C.T. Bowers, J. R. Machacek, L.W. Burggraf, Influence of nano-sized SiC on the laser powder bed

- fusion of molybdenum, *Crystals* 12 (2022) 1276, <https://doi.org/10.3390/cryst12091276>.
- [40] M. Higashi, T. Ozaki, Selective laser melting of pure molybdenum: evolution of defect and crystallographic texture with process parameters, *Mater. Des.* 191 (2020) 108588, <https://doi.org/10.1016/j.matdes.2020.108588>.
- [41] B. Guan, X. Yang, J. Tang, L. Qin, M. Xu, Y. Yan, Y. Cheng, G. Le, Strategies to reduce pores and cracks of molybdenum fabricated by selective laser melting, *Int. J. Refract. Met. Hard Mater.* 112 (2023) 106123, <https://doi.org/10.1016/j.ijrmhm.2023.106123>.
- [42] A. Iveković, N. Omidvari, B. Vrancken, K. Lietaert, L. Thijs, K. Vanmeensel, J. Vleugels, J.-P. Kruth, Selective laser melting of tungsten and tungsten alloys, *Int. J. Refract. Met. Hard Mater.* 72 (2018) 27–32, <https://doi.org/10.1016/j.ijrmhm.2017.12.005>.
- [43] D. Wang, C. Yu, J. Ma, W. Liu, Z. Shen, Densification and crack suppression in selective laser melting of pure molybdenum, *Mater. Des.* 129 (2017) 44–52, <https://doi.org/10.1016/j.matdes.2017.04.094>.
- [44] A.V. Müller, G. Schlick, R. Neu, C. Anstätt, T. Klimkait, J. Lee, B. Pascher, M. Schmitt, C. Seidel, Additive manufacturing of pure tungsten by means of selective laser beam melting with substrate preheating temperatures up to 1000 °C, *Nucl. Mater. Energy* 19 (2019) 184–188, <https://doi.org/10.1016/j.nme.2019.02.034>.
- [45] K.-H. Leitz, P. Singer, A. Plankensteiner, B. Tabernig, H. Kestler, L.S. Sigl, Multi-physical simulation of selective laser melting, *Met. Powder Rep.* 72 (2017) 331–338, <https://doi.org/10.1016/j.mprp.2016.04.004>.
- [46] K.-H. Leitz, C. Grohs, P. Singer, B. Tabernig, A. Plankensteiner, H. Kestler, L.S. Sigl, Fundamental analysis of the influence of powder characteristics in Selective Laser Melting of molybdenum based on a multi-physical simulation model, *Int. J. Refract. Met. Hard Mater.* 72 (2018) 1–8, <https://doi.org/10.1016/j.ijrmhm.2017.11.034>.
- [47] Y. Wu, M. Li, J. Wang, Y. Wang, X. An, H. Fu, H. Zhang, X. Yang, Q. Zou, Powder-bed-fusion additive manufacturing of molybdenum: process simulation, optimization, and property prediction, *Addit. Manuf.* 58 (2022) 103069, <https://doi.org/10.1016/j.addma.2022.103069>.
- [48] P. Bajaj, J. Wright, I. Todd, E.A. Jäggle, Predictive process parameter selection for Selective Laser Melting Manufacturing: applications to high thermal conductivity alloys, *Addit. Manuf.* 27 (2019) 246–258, <https://doi.org/10.1016/j.addma.2018.12.003>.
- [49] S.E. Brika, M. Letenneur, C.A. Dion, V. Brailovski, Influence of particle morphology and size distribution on the powder flowability and laser powder bed fusion manufacturability of Ti-6Al-4V alloy, *Addit. Manuf.* 31 (2020) 100929, <https://doi.org/10.1016/j.addma.2019.100929>.
- [50] H. Hügel, F. Dausinger, *Interaction phenomena*, in: *Handb. EuroLaser Acad.*, Dieter Schöcker, Springer, New York, NY, 1998, pp. 1–102.
- [51] K. Bala, P.R. Pradhan, N.S. Saxena, M.P. Saksena, Effective thermal conductivity of copper powders, *J. Phys. Appl. Phys.* 22 (1989) 1068–1072, <https://doi.org/10.1088/0022-3727/22/8/009>.
- [52] J. Gan, K. Du, X. Ji, Y. Huang, K. Li, Y. Li, X. Zhao, Y. Guo, M. Zhao, C. Wang, H. Chen, D. Zhuang, F. Lin, Q. Gong, Research about the microcrack mechanisms in molybdenum and corresponding suppression strategies during laser additive manufacturing process, *Materialia* 36 (2024) 102173, <https://doi.org/10.1016/j.mtla.2024.102173>.
- [53] C. Tan, K. Zhou, W. Ma, B. Attard, P. Zhang, T. Kuang, Selective laser melting of high-performance pure tungsten: parameter design, densification behavior and mechanical properties, *Sci. Technol. Adv. Mater.* 19 (2018) 370–380, <https://doi.org/10.1080/14686996.2018.1455154>.
- [54] S.H. Kang, H.-H. Jin, J. Jang, Y.S. Choi, K.H. Oh, D.C. Foley, X. Zhang, A quantitative evaluation of microstructure by electron back-scattered diffraction pattern quality variations, *Microsc. Microanal.* 19 (2013) 83–88, <https://doi.org/10.1017/S1431927613012397>.
- [55] F.J. Humphreys, M. Hatherly, *Recrystallization and Related Annealing Phenomena*, Pergamon, Oxford New York Tokyo, 1995.
- [56] K. Yvell, T.M. Grehk, P. Hedström, A. Borgenstam, G. Engberg, EBSD analysis of surface and bulk microstructure evolution during interrupted tensile testing of a Fe-19Cr-12Ni alloy, *Mater. Char.* 141 (2018) 8–18, <https://doi.org/10.1016/j.matchar.2018.04.035>.
- [57] J. Wheeler, Z. Jiang, D.J. Prior, J. Tullis, M.R. Drury, P.W. Trimby, From geometry to dynamics of microstructure: using boundary lengths to quantify boundary misorientations and anisotropy, *Tectonophysics* 376 (2003) 19–35, <https://doi.org/10.1016/j.tecto.2003.08.007>.
- [58] E04 Committee, Practice for Determining Average Grain Size Using Electron Backscatter Diffraction (EBSD) in Fully Recrystallized Polycrystalline Materials, (n.d.), <https://doi.org/10.1520/E2627-13R19>.
- [59] E28 Committee, Test Methods of Compression Testing of Metallic Materials at Room Temperature, (n.d.), <https://doi.org/10.1520/E0009-09>.
- [60] E28 Committee, Practice for Compression Tests of Metallic Materials at Elevated Temperatures with Conventional or Rapid Heating Rates and Strain Rates, (n.d.), <https://doi.org/10.1520/E0209-18>.
- [61] S. Moylan, A. Cooke, K. Jurens, J. Slotwinski, M.A. Donmez, A Review of Test Artifacts for Additive Manufacturing, National Institute of Standards and Technology, 2012, <https://doi.org/10.6028/NIST.IR.7858>.
- [62] S. Kou, Basic solidification concepts, in: *Weld. Metall.*, John Wiley & Sons, Ltd, 2002, pp. 143–169, <https://doi.org/10.1002/0471434027.ch6>.
- [63] L. Kaserer, J. Braun, J. Stajkovic, K.-H. Leitz, B. Tabernig, P. Singer, I. Letofsky-Papst, H. Kestler, G. Leichtfried, Fully dense and crack free molybdenum manufactured by Selective Laser Melting through alloying with carbon, *Int. J. Refract. Met. Hard Mater.* 84 (2019) 105000, <https://doi.org/10.1016/j.ijrmhm.2019.105000>.
- [64] B10 Committee, Specification for Molybdenum and Molybdenum Alloy Bar, Rod, and Wire, ASTM International, n.d. <https://doi.org/10.1520/B0387-18>.
- [65] P. Fernandez-Zelaia, C. Ledford, S. Kim, Q. Campbell, J.O. Rojas, A.M. Rossy, M. Kirka, Mechanical behavior of additively manufactured molybdenum and fabrication of microtextured composites, *JOM* 74 (2022) 3316–3328, <https://doi.org/10.1007/s11837-022-05379-w>.
- [66] R.P. Carreker, R.W. Guard, Tensile deformation of molybdenum as a function of temperature and strain rate, *JOM* 8 (1956) 178–184, <https://doi.org/10.1007/BF03377669>.
- [67] A.T. Nelson, E.S. Sooby, Y.-J. Kim, B. Cheng, S.A. Maloy, High temperature oxidation of molybdenum in water vapor environments, *J. Nucl. Mater.* 448 (2014) 441–447, <https://doi.org/10.1016/j.jnucmat.2013.10.043>.
- [68] P. Fernandez-Zelaia, C. Ledford, E.A.I. Ellis, Q. Campbell, A.M. Rossy, D. N. Leonard, M.M. Kirka, Crystallographic texture evolution in electron beam melting additive manufacturing of pure Molybdenum, *Mater. Des.* 207 (2021) 109809, <https://doi.org/10.1016/j.matdes.2021.109809>.
- [69] T. Ramakrishnan, A. Kumar, P. Hudon, M. Brochu, Laser powder bed fusion additive manufacturing of Mo and TZM exoskeleton with Cu infiltration for new heat sinks configuration, *Adv. Eng. Mater.* 26 (2024) 2301409, <https://doi.org/10.1002/adem.202301409>.
- [70] A.H. Cottrell, B.A. Bilby, Dislocation theory of yielding and strain ageing of iron, *Proc. Phys. Soc. Sect. A* 62 (1949) 49–62, <https://doi.org/10.1088/0370-1298/62/1/308>.
- [71] P. Túry, S. Krausz, Effect of molecular nitrogen on molybdenum at high temperatures, *Nature* 138 (1936), <https://doi.org/10.1038/138331a0>, 331–331.
- [72] R.H. Cooper Jr., E.E. Hoffman, *Refractory Alloy Technology for Space Nuclear Power Applications*, Oak Ridge National Laboratory and U.S. Department of Energy, Oak Ridge Operations, Oak Ridge, Tennessee, USA, 1984.
- [73] P. Rebesan, *Characterization of Molybdenum Produced by Laser Powder Bed Fusion for the High-Temperature Ion Sources of the INFN SPES Facility*, Politecnico di Milano, 2022.
- [74] Q. Shi, W. Du, F. Qin, C. Tan, K. Khanlari, H. Xie, X. Liu, A. Wu, Pure tungsten fabricated by laser powder bed fusion with subsequent hot isostatic pressing: microstructural evolution, mechanical properties, and thermal conductivity, *J. Mater. Eng. Perform.* 32 (2023) 10910–10923, <https://doi.org/10.1007/s11665-023-07891-9>.